

Using the Starlight Polarization Efficiency Integral to Constrain Shapes and Porosities of Interstellar Grains

B. T. Draine and Brandon S. Hensley to

Department of Astrophysical Sciences, Princeton University, Princeton, NJ 08544-1001, USA; draine@astro.princeton.edu Received 2020 December 28; revised 2021 April 14; accepted 2021 May 10; published 2021 September 24

A hetract

We have developed a new method for using the observed starlight polarization and polarized submillimeter emission to constrain the shapes and porosities of interstellar grains. We first present the modified picket-fence approximation and verify that it is sufficiently accurate for modeling starlight polarization. We then introduce the observed starlight polarization integral $\Pi_{\rm obs}$ as a measure of the overall strength of the observed polarization of starlight, and the starlight polarization efficiency integral Φ to characterize the effectiveness of different grain types for producing polarization of starlight. The ratio $\Pi_{\rm obs}/\Phi$ determines the mass-weighted alignment $\langle f_{\rm align} \rangle$ of the grains. Approximating the aligned grains in the ISM as spheroids, we use $\Pi_{\rm obs}/\Phi$ to show that the observed starlight polarization constrains the grains to have a minimum degree of asphericity. For porosity $\mathcal{P}=0$, the minimum axial ratio is ~ 1.4 for oblate spheroids, or ~ 1.8 for prolate spheroids. If the grains are porous, more extreme axial ratios are required. The same grains that produce the starlight polarization are able to provide the observed polarized emission at submillimeter wavelengths but with further limits on shape and porosity. Porosities $\mathcal{P}\gtrsim 0.75$ are ruled out. If interstellar grains can be approximated by "astrodust" spheroids, we predict the ratio of $10~\mu m$ polarization to starlight polarization p_V : $p(10~\mu m)/p_V=0.219\pm0.029$. For Cyg OB2-12, we predict $p(10~\mu m)=(2.1\pm0.3)\%$, which should be observable.

Unified Astronomy Thesaurus concepts: Dust continuum emission (412); Starlight polarization (1571); Silicate grains (1456); Far infrared astronomy (529); Interstellar dust extinction (837)

1. Introduction

The polarization of starlight was discovered serendipitously in 1948 (Hall 1949; Hiltner 1949a) and immediately attributed to linear dichroism of the interstellar medium (ISM) arising from aligned dust grains. In addition to polarizing starlight from the far-ultraviolet to the near-infrared, the aligned grains also emit polarized submillimeter radiation (Planck Collaboration Int. XIX. 2015) and, on suitable sightlines, produce measurable polarization of the $10\,\mu\mathrm{m}$ silicate feature in absorption (e.g., Dyck et al. 1973; Wright et al. 2002). Despite many decades of observational and theoretical study, the physics of grain alignment remains uncertain (see the review by Andersson et al. 2015). Irrespective of the aligning mechanisms, observations of polarized extinction and emission can be used to constrain possible grain shapes, porosities, and degree of alignment.

For a given grain shape, porosity, size, and wavelength λ , cross sections for absorption and scattering depend on the grain orientation relative to the propagation direction \hat{k} and polarization E of the incident radiation. For radiative transfer calculations, these cross sections need to be averaged over the actual distribution of grain orientations. Because computing cross sections for nonspherical grains with sizes comparable to the wavelength continues to be numerically challenging, approximate methods are desirable. A frequently used approach is to approximate the orientation-averaged cross sections by a simple weighted average of cross sections for grains with so-called "picket-fence" alignment (Greenberg 1968). For example, in modeling the polarization of the BNKL region of OMC-1, Dyck & Beichman (1974) considered prolate spheroidal grains with long axes lying in the plane of the sky, with a

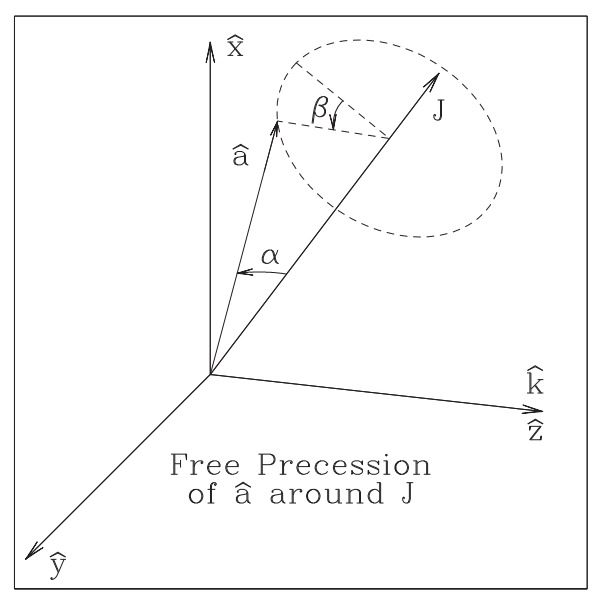
fraction of the spheroids perfectly aligned. In the present paper, we employ a different but still simple treatment, which we refer

Previous studies of the wavelength-dependent polarization of starlight have solved for both the grain size distribution and $f_{\rm align}(a)$ (Kim & Martin 1995; Draine & Allaf-Akbari 2006; Draine & Fraisse 2009; Siebenmorgen et al. 2014; Fanciullo et al. 2017; Guillet et al. 2018) for different assumed grain shapes, but this approach can be very time-consuming. The observed starlight polarization integral $\Pi_{\rm obs}$ —an integral over the observed starlight polarization—can be combined with the starlight polarization efficiency integral Φ to determine $\langle f_{\rm align} \rangle$ without solving for the size distribution or $f_{\rm align}(a)$. An upper bound on $\langle f_{\rm align} \rangle$ then leads to a lower bound on the axial ratio of the grains. The polarized submillimeter emission observed by Planck provides an additional constraint, further limiting the allowed values of both porosity and grain shape.

The paper is organized as follows. In Section 2, we review averaging over spinning, precessing spheroids, and in Section 3 we present the MPFA for estimating orientational averages.

to as the "modified picket-fence approximation" (MPFA). We generalize the Dyck & Beichman (1974) treatment to spinning spheroids, and consider the distribution of symmetry axes in three dimensions. The resulting orientation-averaged cross sections are exact in the long-wavelength limit, and we show that they also provide reasonable accuracy for wavelengths comparable to the grain size. The degree of alignment of interstellar grains is characterized by a size-dependent fractional alignment $f_{\text{align}}(a)$, where a is a measure of the grain size, and a corresponding mass-weighted fractional alignment $\langle f_{\text{align}} \rangle$. The polarization at long wavelengths $\lambda \gtrsim 10 \, \mu \text{m}$ is determined by the grain shape and $\langle f_{\text{align}} \rangle$, but at optical wavelengths, the wavelength dependent polarization depends on both the size distribution and $f_{\text{align}}(a)$.

¹ Spitzer Fellow.



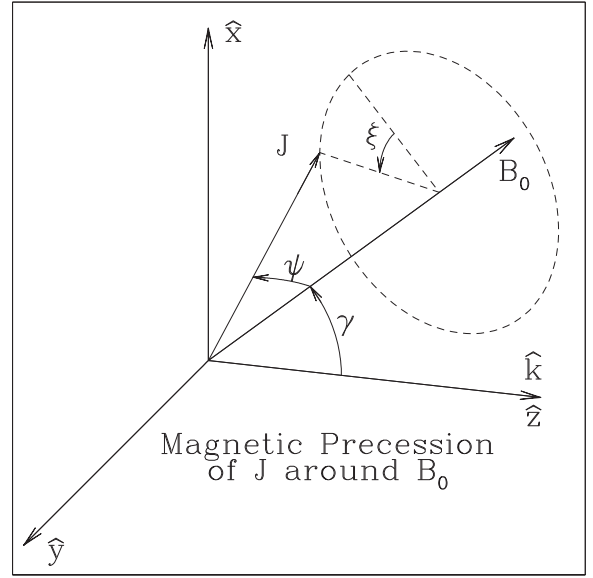


Figure 1. Left: spheroid symmetry axis \hat{a} precesses around angular momentum J. Right: J precesses around magnetic field B_0 .

The MPFA is tested in Section 4. In Sections 5 and 6, we review the observed polarization of starlight and define the starlight polarization efficiency integral Φ for dust grains of specified shape and composition, and the observed starlight polarization integral $\Pi_{\rm obs}$. In Section 7, we define the effective polarizing wavelength $\lambda_{\rm p,eff}$, and we deduce the characteristic size $a_{\rm char}$ of the grains responsible for the observed polarization of starlight. The width of the polarization profile is discussed in Section 8. In Section 9, we show how the mass-weighted alignment fraction $\langle f_{\rm align} \rangle$ can be estimated from the ratio $\Pi_{\rm obs}/\Phi$.

Approximating the grains by spheroids, polarized submillimeter emission from the aligned dust grains is discussed in Section 10; the strength of the observed polarized submillimeter emission leads to a limited domain of allowed shapes and porosities. Polarization in the $10\,\mu\mathrm{m}$ silicate feature is discussed in Section 11, where we calculate the $10\,\mu\mathrm{m}$ polarization per starlight polarization and predict $p(10\,\mu\mathrm{m}) = (2.1 \pm 0.3)\%$ toward Cyg OB2-12. We discuss our conclusions in Section 12. Our principal results are summarized in Section 13.

2. Orientational Averaging for Spinning, Precessing Spheroids

2.1. General Considerations

Interstellar grains spin rapidly, with frequencies ranging from kilohertz up to gigahertz for the smallest particles. Let $0 \le \psi \le \pi/2$ be the angle between the angular momentum J and the local (static) magnetic field B_0 . If $\psi \ne 0$, J will precess around B_0 as the result of the torque exerted on the grain's magnetic moment. For magnetic moments induced by the Barnett effect (Dolginov & Mytrophanov 1976), the "magnetic precession" period in the ISM is relatively short, $\sim 1(a/0.1~\mu\text{m})^2$ yr (Draine & Weingartner 1997). For radiative transfer calculations, cross sections must be averaged over the population of spinning and precessing grains (Greenberg 1968).

Consider axially symmetric grains (e.g., spheroids) with symmetry axis \hat{a} . There are two "alignment angles": the angle α between \hat{a} and J measuring the "internal alignment" of the grain body with J and the angle ψ measuring the alignment of J

with B_0 (see Figure 1). "Perfect" spinning alignment has the grain's short axis aligned with J (the minimum energy state for fixed J) and J aligned with B_0 . Here we allow for imperfect alignment, averaging over the distributions of α and ψ .

On short timescales, the grain motion is approximated by free rotation of a rigid body (nicely treated by Landau & Lifshitz 1976). For a body with axial symmetry, the symmetry axis \hat{a} undergoes free precession around the fixed vector J, with a constant angle α between \hat{a} and J. J precesses around the magnetic field B_0 . On longer timescales, nonrigidity matters; α may vary as internal processes exchange energy between vibrational and rotational degrees of freedom (see Weingartner et al. 2021, and references therein). On even longer timescales, the alignment angle ψ may vary as the result of changes in the angular momentum J, with alignment mechanisms such as paramagnetic dissipation (Davis & Greenstein 1951) acting to reduce ψ .

Let unit vectors \hat{x} , \hat{y} , \hat{z} define inertial coordinates. Let B_0 lie in the $\hat{z} - \hat{x}$ plane, with γ the angle between B_0 and the direction of propagation \hat{z} (see Figure 1).

Averaging over rotation, free precession, and magnetic precession (see Appendix A), we obtain

$$\langle (\hat{\boldsymbol{a}} \cdot \hat{\boldsymbol{x}})^2 \rangle = \frac{1}{3} + \langle R \rangle \left(\sin^2 \gamma - \frac{1}{3} \right),$$
 (1)

$$\langle (\hat{\boldsymbol{a}} \cdot \hat{\boldsymbol{y}})^2 \rangle = \frac{1}{3} - \frac{\langle R \rangle}{3},$$
 (2)

$$\langle (\hat{a} \cdot \hat{z})^2 \rangle = \frac{1}{3} + \langle R \rangle \left(\cos^2 \gamma - \frac{1}{3} \right),$$
 (3)

where $\langle ... \rangle$ denotes averaging over rotation, free precession, magnetic precession, and the distributions of the alignment angles α and ψ . The "reduction factor" (Greenberg 1968)

$$\langle R \rangle \equiv \left\langle \left(\frac{3}{2} \cos^2 \psi - \frac{1}{2} \right) \left(\frac{3}{2} \cos^2 \alpha - \frac{1}{2} \right) \right\rangle_{\alpha\psi}$$
 (4)

is averaged over the distributions of the internal alignment angle α and the magnetic alignment angle ψ . Equation (4)

allows for the possibility that α and ψ may be correlated. Randomly oriented grains have $\langle R \rangle = 0$.

Under interstellar conditions, grains may undergo "suprathermal rotation" (Purcell 1975, 1979) with rotational kinetic energy $E_{\rm rot} \gg k_{\rm B}T_{\rm gr}$, where $T_{\rm gr}$ is the grain temperature. When this is the case, internal dissipation in the grain will tend to minimize its rotational kinetic energy at fixed J, aligning the short axis of the body with J. For oblate spheroids, this means $\alpha \to 0$; for prolate spheroids, $\alpha \to \pi/2$.

Davis & Greenstein (1951) showed that paramagnetic dissipation in a grain spinning in a static magnetic field B_0 will exert a torque on the grain that acts to bring J into alignment with B_0 . Thus, in the absence of other torques, $\psi \to 0$.

Therefore, "perfect" alignment has $\langle R \rangle = 1$ for oblate spheroids and $\langle R \rangle = -1/2$ for prolate spheroids. To measure how close the alignment is to "perfect," we define the "alignment factor"

$$f_{\text{align}} \equiv \begin{cases} \langle R \rangle & \text{for oblate spheroids} \\ -2 \langle R \rangle & \text{for prolate spheroids.} \end{cases}$$
 (5)

Randomly oriented spheroids have $f_{\rm align} = 0$. Optimally oriented spinning spheroids have $f_{\rm align} = 1$. The actual alignment factor will be $f_{\rm align} < 1$, because there will be processes (e.g., collisions with gas atoms) acting to randomize the direction of J.

2.2. Cross Sections

Consider grains with rotational symmetry around a symmetry axis \hat{a} and reflection symmetry through a plane perpendicular to \hat{a} . For simplicity, we consider spheroids, but the results in this section apply to cylinders and other shapes with axial and reflection symmetry.

Let photons be propagating in the direction $\hat{k} = \hat{z}$, and let Θ be the angle between \hat{k} and \hat{a} . Cross sections for absorption or scattering of light with polarization E depend on Θ and the orientation of E with respect to \hat{a} . Let $C_E(\Theta)$ be the cross section for E in the $\hat{k} - \hat{a}$ plane and $C_H(\Theta)$ be the cross section for the magnetic field E in the E plane. The cross sections for incident light polarized in the E and E directions are

$$C_{x}(\Theta) = \frac{(\hat{\boldsymbol{a}} \cdot \hat{\boldsymbol{x}})^{2}}{(\hat{\boldsymbol{a}} \cdot \hat{\boldsymbol{x}})^{2} + (\hat{\boldsymbol{a}} \cdot \hat{\boldsymbol{y}})^{2}} C_{E}(\Theta) + \frac{(\hat{\boldsymbol{a}} \cdot \hat{\boldsymbol{y}})^{2}}{(\hat{\boldsymbol{a}} \cdot \hat{\boldsymbol{x}})^{2} + (\hat{\boldsymbol{a}} \cdot \hat{\boldsymbol{y}})^{2}} C_{H}(\Theta),$$
(6)

$$C_{y}(\Theta) = \frac{(\hat{\boldsymbol{a}} \cdot \hat{\boldsymbol{y}})^{2}}{(\hat{\boldsymbol{a}} \cdot \hat{\boldsymbol{x}})^{2} + (\hat{\boldsymbol{a}} \cdot \hat{\boldsymbol{y}})^{2}} C_{E}(\Theta) + \frac{(\hat{\boldsymbol{a}} \cdot \hat{\boldsymbol{x}})^{2}}{(\hat{\boldsymbol{a}} \cdot \hat{\boldsymbol{x}})^{2} + (\hat{\boldsymbol{a}} \cdot \hat{\boldsymbol{y}})^{2}} C_{H}(\Theta), \tag{7}$$

with $\Theta \equiv \arccos(\hat{a} \cdot \hat{z})$. Here C can denote a cross section for absorption, scattering, or extinction. For radiative transfer calculations, the scattering and absorption cross sections must

be averaged over the distribution of grain orientations:

$$\langle C_x \rangle = \left\langle \frac{(\hat{\boldsymbol{a}} \cdot \hat{\boldsymbol{x}})^2}{(\hat{\boldsymbol{a}} \cdot \hat{\boldsymbol{x}})^2 + (\hat{\boldsymbol{a}} \cdot \hat{\boldsymbol{y}})^2} C_E(\Theta) \right\rangle + \left\langle \frac{(\hat{\boldsymbol{a}} \cdot \hat{\boldsymbol{y}})^2}{(\hat{\boldsymbol{a}} \cdot \hat{\boldsymbol{x}})^2 + (\hat{\boldsymbol{a}} \cdot \hat{\boldsymbol{y}})^2} C_H(\Theta) \right\rangle, \tag{8}$$

$$\langle C_{y} \rangle = \left\langle \frac{(\hat{\boldsymbol{a}} \cdot \hat{\boldsymbol{y}})^{2}}{(\hat{\boldsymbol{a}} \cdot \hat{\boldsymbol{x}})^{2} + (\hat{\boldsymbol{a}} \cdot \hat{\boldsymbol{y}})^{2}} C_{E}(\Theta) \right\rangle + \left\langle \frac{(\hat{\boldsymbol{a}} \cdot \hat{\boldsymbol{x}})^{2}}{(\hat{\boldsymbol{a}} \cdot \hat{\boldsymbol{x}})^{2} + (\hat{\boldsymbol{a}} \cdot \hat{\boldsymbol{y}})^{2}} C_{H}(\Theta) \right\rangle, \tag{9}$$

$$\frac{\langle C_{y} \rangle - \langle C_{x} \rangle}{2} = \left\langle \frac{\left[(\hat{\boldsymbol{a}} \cdot \hat{\boldsymbol{x}})^{2} - (\hat{\boldsymbol{a}} \cdot \hat{\boldsymbol{y}})^{2} \right] \left[C_{H}(\Theta) - C_{E}(\Theta) \right]}{\left[(\hat{\boldsymbol{a}} \cdot \hat{\boldsymbol{x}})^{2} + (\hat{\boldsymbol{a}} \cdot \hat{\boldsymbol{y}})^{2} \right]} \frac{1}{2} \right\rangle. \tag{10}$$

In Equations (8–10), $\langle ... \rangle$ denotes time averages over rotation, free precession, and magnetic precession for a single grain with given α and ψ values (see Equations (A10) and (A11)), averaged over the distribution of α and ψ for grains of this size and shape. In the ISM, this should then be followed by averaging over the distribution of grain sizes and shapes.

The optical depths for radiation linearly polarized in the \hat{x} and \hat{y} directions are

$$\tau_x = N_d \langle C_x \rangle, \tag{11}$$

$$\tau_{v} = N_d \langle C_{v} \rangle, \tag{12}$$

where $N_d \equiv \int n_d dz$ is the dust column density. Dichroic extinction will cause initially unpolarized light to become linearly polarized in the \hat{x} direction, with fractional polarization

$$p = \frac{e^{-\tau_x} - e^{-\tau_y}}{e^{-\tau_y} + e^{-\tau_x}}$$
 (13)

$$\rightarrow \frac{\langle C_y \rangle - \langle C_x \rangle}{2} N_d \text{ for } |\tau_x - \tau_y| \ll 1.$$
 (14)

2.3. Cross Sections in the Rayleigh Limit

Let $a_{\rm eff} \equiv (3V/4\pi)^{1/3}$ be the "effective radius" for a grain of volume V. In the Rayleigh limit $(a_{\rm eff}/\lambda \to 0)$, the cross sections can be written²

$$C_E(\Theta, \lambda) = \cos^2 \Theta C_E(0, \lambda) + \sin^2 \Theta C_E(90^\circ, \lambda),$$
 (15)

$$C_H(\Theta, \lambda) = \cos^2 \Theta C_H(0, \lambda) + \sin^2 \Theta C_H(90^\circ, \lambda),$$
 (16)

and Equations (8-10) become

$$\langle C_x \rangle = \langle (\hat{\boldsymbol{a}} \cdot \hat{\boldsymbol{x}})^2 \rangle C_E(90^\circ) + \langle (\hat{\boldsymbol{a}} \cdot \hat{\boldsymbol{y}})^2 \rangle C_H(90^\circ) + \langle (\hat{\boldsymbol{a}} \cdot \hat{\boldsymbol{z}})^2 \rangle C_E(0),$$
 (17)

$$\langle C_{y} \rangle = \langle (\hat{\boldsymbol{a}} \cdot \hat{\boldsymbol{x}})^{2} \rangle C_{H}(90^{\circ}) + \langle (\hat{\boldsymbol{a}} \cdot \hat{\boldsymbol{y}})^{2} \rangle C_{E}(90^{\circ}) + \langle (\hat{\boldsymbol{a}} \cdot \hat{\boldsymbol{z}})^{2} \rangle C_{E}(0).$$
 (18)

$$C_{\text{abs}} = \frac{4\pi\omega}{c} \frac{\sum_{j=1}^{3} |E_j|^2 \operatorname{Im}(\alpha_{jj})}{\sum_{i=1}^{3} |E_i|^2},$$

and Equations (15) and (16) follow directly

 $[\]overline{^2}$ In the electric dipole limit, interaction of a grain with an applied E field is characterized by the complex polarizability tensor α_{ij} (Draine & Lee 1984). Choosing coordinates where α_{ij} is diagonalized,

Define the polarization cross section

$$C_{\text{pol}}(\lambda) \equiv \begin{cases} \frac{[C_H(90^\circ, \lambda) - C_E(90^\circ, \lambda)]}{2} & \text{for oblate spheroids} \\ \frac{[C_E(90^\circ, \lambda) - C_H(90^\circ, \lambda)]}{4} & \text{for prolate spheroids,} \end{cases}$$
(19)

the "random orientation" extinction cross section

$$C_{\text{ran}}(\lambda) \equiv \frac{[C_E(0, \lambda) + C_E(90^{\circ}, \lambda) + C_H(90^{\circ}, \lambda)]}{3},$$
 (20)

and the "anisotropic" extinction cross section

distributed over just three different "picket-fence" orientations, with the symmetry axis \hat{a} along either the \hat{x} , \hat{y} , or \hat{z} axes. It is natural to use the weighting factors that give exact results in the Rayleigh limit.

The MPFA estimates for linear dichroism and polarizationaveraged extinction are

$$\frac{\langle C_y \rangle - \langle C_x \rangle}{2} \approx C_{\text{pol}}^{\text{MPFA}}(\lambda)$$

$$C_{\text{pol}}^{\text{MPFA}}(\lambda) \equiv f_{\text{align}} \sin^2 \gamma C_{\text{pol}}(\lambda) \tag{24}$$

$$C_{\text{aniso}}(\lambda) \equiv \begin{cases} C_E(0, \lambda) - \frac{[C_E(90^\circ, \lambda) + C_H(90^\circ, \lambda)]}{2} & \text{for oblate spheroids} \\ \frac{[C_E(90^\circ, \lambda) + C_H(90^\circ, \lambda)]}{4} - \frac{C_E(0, \lambda)}{2} & \text{for prolate spheroids.} \end{cases}$$
(21)

A spherical grain has $C_{\rm aniso} = C_{\rm pol} = 0$, but other spheroids will generally have $C_{\rm aniso} \neq 0$ and $C_{\rm pol} \neq 0$. In the Rayleigh limit, we will generally have $C_{\rm aniso} > 0$ and $C_{\rm pol} > 0$ for either oblate or prolate shapes.

Then, for alignment fraction f_{align} (see Equation (5)), we have

$$\frac{\langle C_y \rangle - \langle C_x \rangle}{2} = f_{\text{align}} \sin^2 \gamma \ C_{\text{pol}}(\lambda), \tag{22}$$

$$\frac{\langle C_y \rangle + \langle C_x \rangle}{2} = C_{\text{ran}}(\lambda)$$

$$+ f_{\text{align}} \left(\cos^2 \gamma - \frac{1}{2} \right) C_{\text{aniso}}(\lambda). \tag{23}$$

These results are exact in the Rayleigh limit $a_{\rm eff}/\lambda \rightarrow 0$. Note that in the Rayleigh limit, nonmagnetic spheroids have $C_H(90^\circ) = C_E(0)$, and $C_{\rm aniso} = C_{\rm pol}$. If $C_{\rm aniso} \neq 0$, $f_{\rm align} \neq 0$, and $\cos^2 \gamma \neq 1/3$, we see from Equation (23) that the polarization-averaged extinction differs from $C_{\rm ran}$.

Equations (22) and (23) were derived previously by other authors (e.g., Lee & Draine 1985; Planck Collaboration Int. XX. 2015, Appendix B therein). Here we have generalized $f_{\rm align}$ to allow for imperfect internal alignment. We also distinguish between $C_{\rm aniso}$ and $C_{\rm pol}$ even in the limit $\lambda \gg a_{\rm eff}$ to allow for the possibility of magnetic dipole absorption by magnetic grains (Draine & Hensley 2013).

3. Modified Picket-fence Approximation

Equations (6) and (7) are exact for spheroids (or any other shape with axial and reflection symmetry through the equatorial plane). In the Rayleigh limit, we require only three cross sections to be calculated for each size and wavelength: $C_E(0)$, $C_E(90^\circ)$, and $C_H(90^\circ)$. For finite values of $a_{\rm eff}/\lambda$, accurate evaluation of the averages (Equations (8) and (9)) may require calculation of $C_E(\Theta)$ and $C_H(\Theta)$ for many values of Θ , which can be computationally demanding.

The modified picket-fence approximation (MPFA) consists of approximating $\langle C_x \rangle$ and $\langle C_y \rangle$ using Equations (17) and (18) even when $a_{\rm eff}/\lambda$ is not small, with $\langle C_x \rangle$ and $\langle C_y \rangle$ taken to be suitably weighted averages of the three cross sections $C_E(0)$, $C_E(90^\circ)$, and $C_H(90^\circ)$. This is tantamount to approximating the grains as being

$$\frac{\langle C_y \rangle + \langle C_x \rangle}{2} \approx C_{\text{ext}}^{\text{MPFA}}(\lambda)$$

$$C_{\text{ext}}^{\text{MPFA}}(\lambda) \equiv C_{\text{ran}}(\lambda) + f_{\text{align}} \left(\cos^2 \gamma - \frac{1}{3}\right) C_{\text{aniso}}(\lambda),$$
(25)

with $C_{\text{pol}}(\lambda)$, $C_{\text{ran}}(\lambda)$, and $C_{\text{aniso}}(\lambda)$ defined by Equations (19)–(21).

Greenberg (1968) pointed out that if grains are aligned, the extinction coefficient and "reddening law" will depend on the direction of propagation of light relative to the magnetic field; the attenuation coefficient is anisotropic. The anisotropic part of the extinction is contained in the term $f_{\rm align}\left(\frac{3}{2}\cos^2\gamma-\frac{1}{2}\right)C_{\rm aniso}(\lambda)$. It has not yet been possible to detect this anisotropy in studies of starlight extinction, but it has been detected in thermal emission at submillimeter wavelengths (Hensley et al. 2019); interstellar dust radiates more strongly in directions parallel to B_0 (i.e., $\cos^2\gamma=1$) and more weakly in directions perpendicular to the field $(\cos^2\gamma=0)$.

We refer to Equations (24) and (25) as the "modified" picket-fence approximation to distinguish them from the picket-fence approximation used by Dyck & Beichman (1974, hereafter DB74), who assumed the grain population could be approximated by spheroids in just two orientations: a fraction f_x of the spheroids have a long axis in the \hat{x} direction and a short axis in the \hat{y} direction, and a fraction $1 - f_x$ have a long axis in the \hat{y} direction and a short axis in the \hat{x} direction. With appropriate choices of f_x , the DB74 approach can reproduce the polarization cross section $\langle C_y \rangle - \langle C_x \rangle$ in the long-wavelength limit, but it does not reproduce $\langle C_x \rangle$ or $\langle C_y \rangle$. The MPFA is, in effect, a 3D picket-fence treatment that is exact in the limit $\lambda \gg a_{\rm eff}$.

For finite values of $a_{\rm eff}/\lambda$, the cross sections $C_E(\Theta)$ and $C_H(\Theta)$ have a more complex dependence on Θ than the simple linear dependence on $\cos^2\Theta$ in Equations (15) and (16), but we anticipate that orientational averaging may make $\langle C_x \rangle$ and $\langle C_y \rangle$ relatively insensitive to deviations from the assumed linear dependence on $\cos^2\Theta$. The error in using the MPFA is expected to be most severe when $2\pi a_{\rm eff}/\lambda \approx 1$, the regime where the cross sections $C_E(\Theta)$ and $C_H(\Theta)$ are most strongly

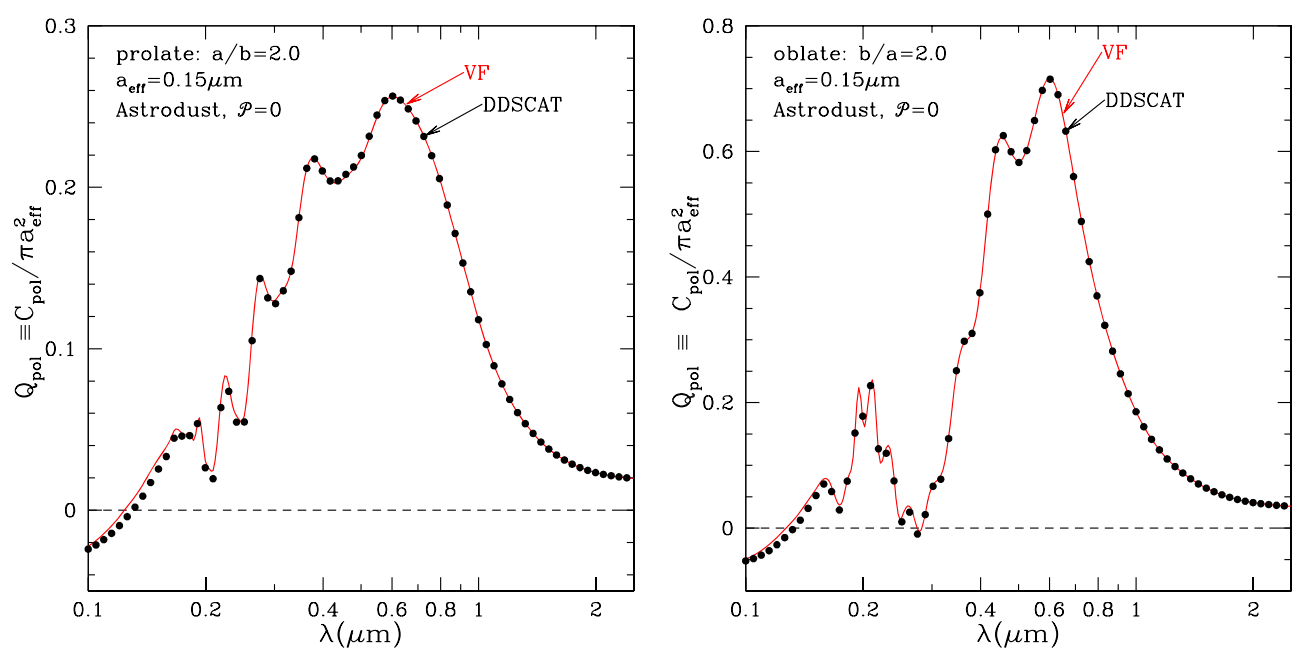


Figure 2. Normalized polarization cross section for $a_{\rm eff} = 0.15~\mu m$ grains composed of "astrodust" material with porosity $\mathcal{P} = 0$. Left: 2:1 prolate spheroid. Right: 2:1 oblate spheroid. Red curve: method of Voshchinnikov & Farafonov (1993) (VF). Black points: DDA calculations (DDSCAT). Agreement is excellent for both oblate and prolate cases.

affected by resonances. The accuracy of the MPFA for $2\pi a_{\rm eff}/\lambda \sim 1$ is tested below.

4. Testing the MPFA

At wavelengths $\lambda \gtrsim 8~\mu m$, submicron grains have $2\pi a_{\rm eff}/\lambda \ll 1$, and the MPFA (Equations (17) and (18)) is known to be accurate. However, at "optical" wavelengths where starlight polarization is measured, $2\pi a_{\rm eff}/\lambda \gtrsim 0.5$, and the accuracy of the MPFA must be checked by comparison to the exact averages in Equations (8) and (9).

When $2\pi a_{\rm eff}/\lambda \gtrsim 0.5$, calculation of scattering and absorption by shapes other than spheres becomes challenging. Electromagnetic absorption and scattering by spheroids can be treated using various approaches, including separation of variables (Asano & Yamamoto 1975; Rogers & Martin 1979; Voshchinnikov & Farafonov 1993), the "extended boundary condition method" (often referred to as the "T-matrix method"; Waterman 1965; Mishchenko 2000, 2020), the "generalized point matching method" (Al-Rizzo & Tranquilla 1995; Weingartner & Jordan 2008), or the discrete dipole approximation (Draine & Flatau 1994). Because the calculations are time-consuming (and become numerically delicate when $2\pi a_{\rm eff}/\lambda \gtrsim 10$), fast methods are desirable, but accuracy must be verified.

To test the MPFA, we need accurate cross sections with which to compare. We consider grains composed of "astrodust" material, using dielectric functions derived by Draine & Hensley (2021). Astrodust is assumed to consist of amorphous silicate material (with nominal composition Mg_{1.3}Fe_{0.3}SiO_{3.6}) mixed with carbonaceous material and other nonsilicate materials, such as Al₂O₃, FeS, Fe₃O₄, and possibly metallic Fe. The silicate material itself accounts for approximately 50% of the mass of the astrodust material (see Draine & Hensley 2021 for

discussion of likely constituents). Astrodust grains may also contain voids, with a void filling factor (i.e., porosity) \mathcal{P} . We consider porosities in the range $0 \leqslant \mathcal{P} \leqslant 0.9$ and various axial ratios b/a. For each choice of \mathcal{P} and b/a, we use the appropriate dielectric function obtained by Draine & Hensley (2021), based on fits to the observed extinction toward Cyg OB2-12 (Hensley & Draine 2020) and estimates of the dust opacity based on observations at other wavelengths (Hensley & Draine 2021).

Absorption, scattering, and extinction cross sections $C_E(0) = C(\hat{k} || \hat{a})$, $C_E(90^\circ) = C(\hat{k} \perp \hat{a}, E || \hat{a})$, and $C_H(90^\circ) = C(\hat{k} \perp \hat{a}, E \perp \hat{a})$ have been calculated for spheroids using the separation of variables method code of Voshchinnikov & Farafonov (1993, hereafter VF). Tabulated results for a range of grain sizes and shapes, wavelengths $\lambda > 912 \text{ Å}$, and a range of porosities are available online.

Figure 2 shows the dimensionless polarization efficiency

$$Q_{\rm pol} \equiv \frac{C_{\rm pol}}{\pi a_{\rm aff}^2} \tag{26}$$

for zero-porosity ($\mathcal{P}=0$) astrodust grains with size $a_{\rm eff}=0.15~\mu{\rm m}$ as a function of vacuum wavelength λ . Results are shown for two independent methods: the separation of variables method code written by Voshchinnikov & Farafonov (1993)⁵ and the discrete dipole approximation (DDA; Draine & Flatau 1994) using the public-domain code DDSCAT.⁶

The DDSCAT calculations were done with N = 265,848 and 277,888 dipoles for b/a = 2 and 0.5, respectively. Figure 2 shows that the DDA and VF results are in excellent agreement, confirming that both methods are accurate.

Figure 2 shows that, for a given axial ratio, oblate spheroids are better polarizers than prolate spheroids; the peak value of

³ Dielectric functions and computed cross sections are available at https://doi.org/10.34770/9ypp-dv78.

⁴ Ibid.

⁵ hom6_5q, available from http://www.astro.spbu.ru/DOP/6-SOFT/SPHEROID/1-SPH_new/.

DDSCAT 7.3.3, available from http://www.ddscat.org.

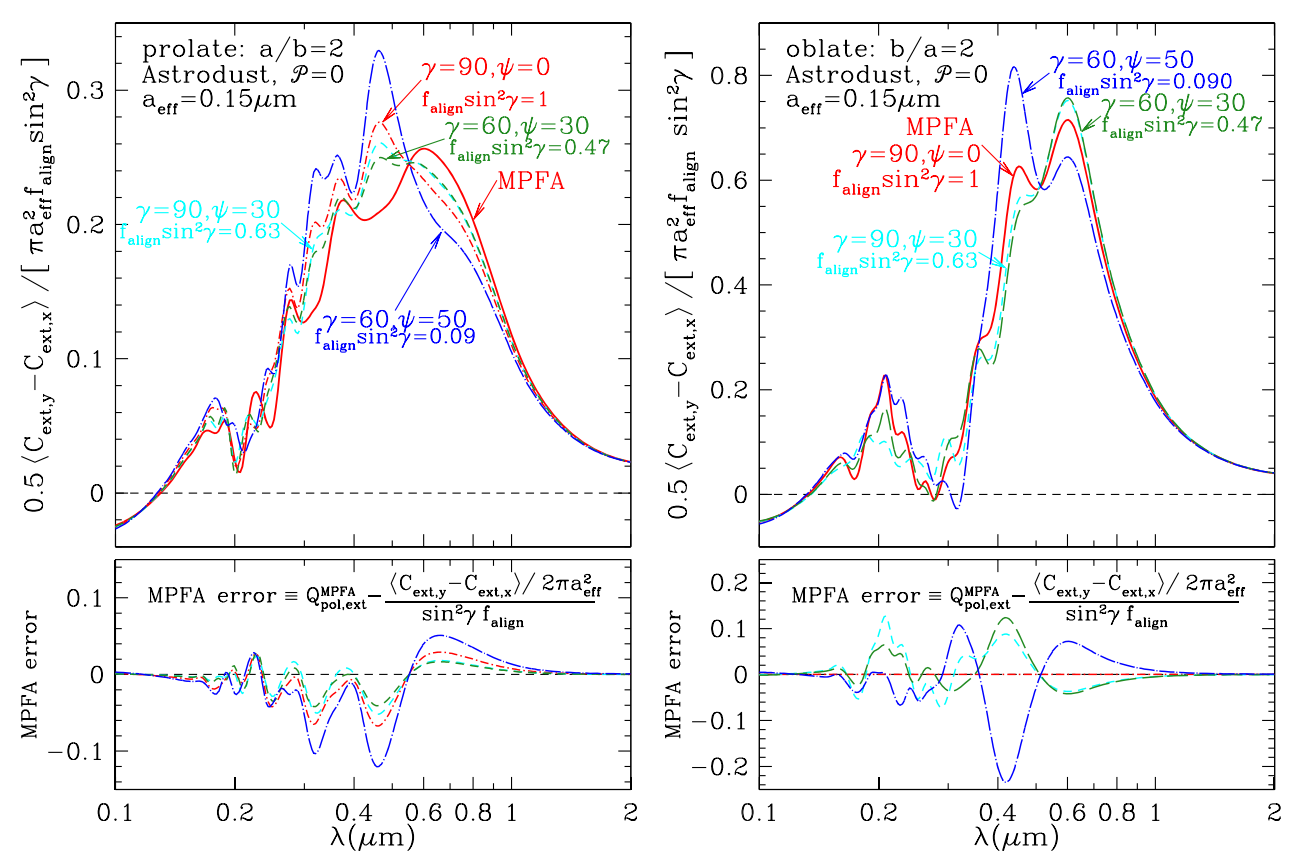


Figure 3. Orientationally averaged cross section for polarization $(1/2)(\langle C_y \rangle - \langle C_x \rangle)$ divided by $\pi a_{\rm eff}^2 f_{\rm align} \sin^2 \gamma$ as a function of wavelength λ . Left: 2:1 prolate grains with $\alpha = 90^\circ$. Right: 2:1 oblate grains with $\alpha = 0$. Grains are spinning with J parallel to the principal axis of the largest moment of inertia, with J precessing around B_0 . Results are shown for four different distributions of grain orientation, labeled by $\gamma =$ angle between B_0 and the line of sight and $\psi =$ angle between J and J and J and J and J are curves labeled "MPFA" correspond to the MPFA. The lower panels show the error in $(\langle C_y \rangle - \langle C_x \rangle)/2\pi a_{\rm eff}^2 f_{\rm align} \sin^2 \gamma$ if the MPFA is used. Note that the errors are both positive and negative and will tend to average out for size distributions.

 $Q_{\rm pol}$ for the 2:1 oblate grain is more than twice the peak value for the 2:1 prolate shape. In addition, the polarization profile for the oblate grain is noticeably narrower than for the prolate shape. This will be discussed further in Section 7.

The results in Figure 2 are essentially exact results for a single orientation. In general, we need to average over a distribution of orientations, and we wish to test the accuracy of the MPFA for such calculations. Rogers & Martin (1979) used a separation of variables method to calculate extinction cross sections for dielectric spheroids. Although they did not call it the MPFA, they tested the accuracy of the MPFA (above Equations (24) and (25)) for the case of 2:1 prolate spheroids with refractive index m=1.33, perfect spinning alignment $(\alpha=\pi/2, \psi=0)$, and a magnetic field in the plane of the sky $(\gamma=\pi/2)$. For the case considered by Rogers & Martin (1979), the MPFA estimates for rotation-averaged cross sections were found to be typically within $\sim 10\%$ of the results obtained by directly averaging the actual cross sections $C_E(\Theta)$ and $C_H(\Theta)$ over grain rotation.

We use DDA calculations to test the accuracy of the MPFA for astrodust spheroids with several distributions of orientations. For all cases, we assume perfect "internal alignment" ($\alpha=0$ for oblate grains, $\alpha=\pi/2$ for prolate grains). Figure 3 shows orientationally averaged optical polarization cross sections as a function of wavelength λ for a 2:1 prolate grain and a 2:1 oblate grain, for four different orientation distributions:

- 1. $\mathbf{B}_0 \perp \hat{\mathbf{k}} \quad (\gamma = 90^\circ)$ and perfect (spinning) alignment $(\psi = 0^\circ)$,
- 2. $\mathbf{B}_0 \perp \hat{\mathbf{k}} \ (\gamma = 90^\circ)$ and $\psi = 30^\circ$ between \mathbf{J} and \mathbf{B}_0 ,
- 3. $\gamma = 60^{\circ}$ between \mathbf{B}_0 and $\hat{\mathbf{k}}$ and $\psi = 30^{\circ}$ between \mathbf{J} and \mathbf{B}_0 , and
- 4. $\gamma = 60^{\circ}$ between \boldsymbol{B}_0 and $\hat{\boldsymbol{k}}$ and $\psi = 50^{\circ}$ between \boldsymbol{J} and \boldsymbol{B}_0 .

To evaluate the orientational averages $\langle C_{\text{ext},x} \rangle$ and $\langle C_{\text{ext},y} \rangle$ using Equations (A10) and (A11), we first calculate $C_{\text{ext},E}(\Theta)$ and $C_{\text{ext},H}(\Theta)$ for 11 values of Θ between zero and $\pi/2$. We then interpolate to obtain $C_{\text{ext},x}$ and $C_{\text{ext},y}$ at the values of Θ needed for the integrals over β and ξ (see Equations (A10) and (A11)).

For each orientation distribution, the orientationally averaged polarization cross sections $\frac{1}{2}\langle C_{\mathrm{ext},y} - C_{\mathrm{ext},x} \rangle$ are normalized by dividing by $\pi a_{\mathrm{eff}}^2 f_{\mathrm{align}} \sin^2 \gamma$. Figure 3 shows that these four distributions have very similar normalized optical polarization profiles, for both the oblate and prolate shapes. The polarization cross sections calculated with the MPFA are also shown.

The MPFA is exact in the limit $\lambda \to \infty$. For $a_{\rm eff} = 0.15 \, \mu {\rm m}$, the MPFA is quite accurate for $\lambda > 1 \, \mu {\rm m}$, $(2\pi a_{\rm eff}/\lambda < 1)$, as shown in Figure 3.

For spheroids, the MPFA gives the exact result for the special cases $\alpha=0,\ \psi=0,$ and $\gamma=0^{\circ}$ or $90^{\circ},$ which includes the case $\gamma=90^{\circ},\ \psi=0$ for the oblate example in Figure 3, but for other cases, the orientational averages depart from the

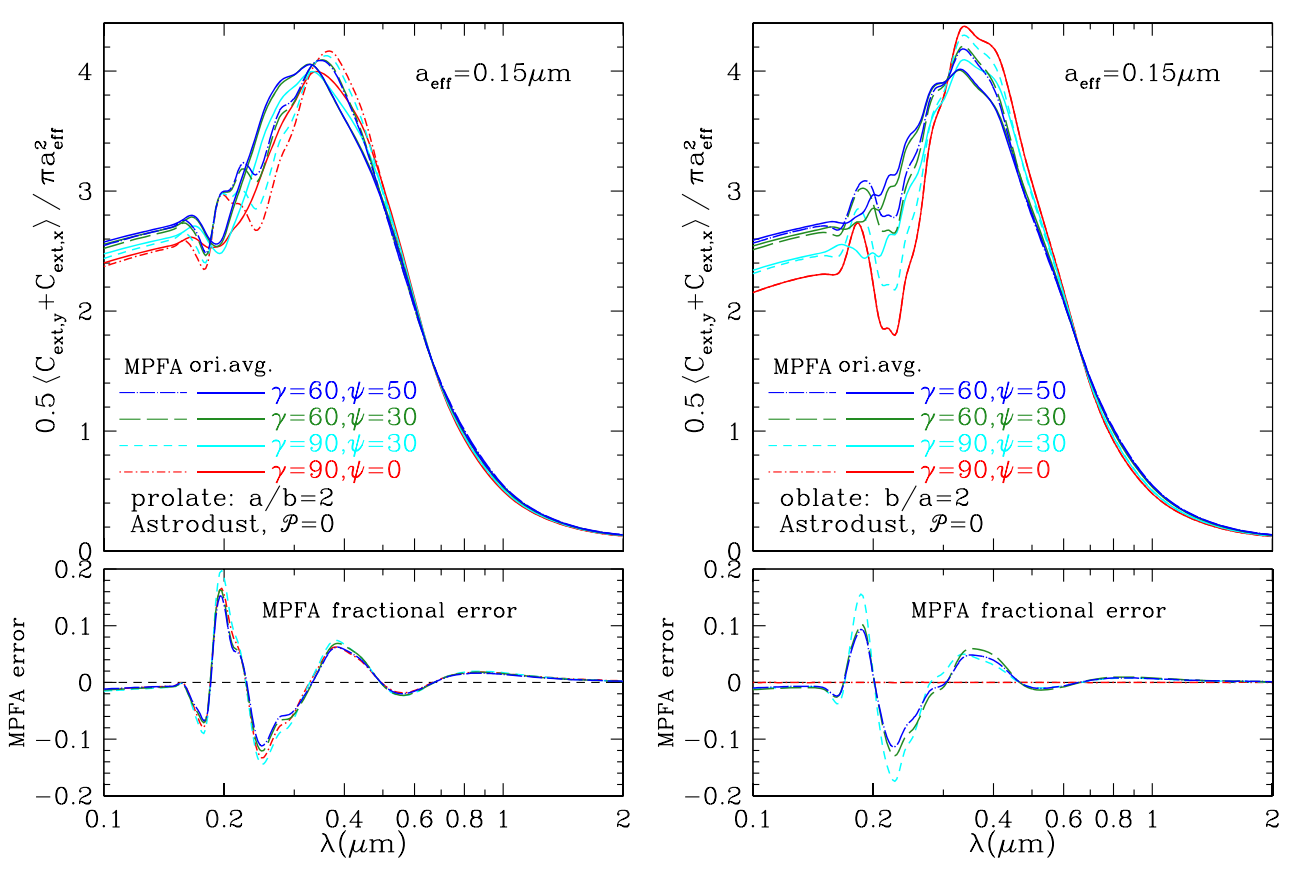


Figure 4. Upper panels: orientation-averaged extinction efficiency factor for unpolarized light for 2:1 spheroids for four different orientation distributions. Lower panels: fractional error for MPFA. All cases are for perfect internal alignment ($\alpha=0$ for oblate, $\alpha=90^{\circ}$ for prolate). For oblate spheroids with $\alpha=0$, the MPFA is exact for $\gamma=90$, $\psi=0$.

MPFA for $\lambda \lesssim 1~\mu m$. The modest oscillatory behavior seen in Figure 3 will be suppressed when averaging over realistic distributions of $a_{\rm eff}$ and ψ , and we expect the MPFA to provide a good approximation after such averaging.

Orientation-averaged cross sections for extinction of unpolarized light are shown in Figure 4 for the same examples as in Figure 3. Once again, we see that the MPFA is exact in the long-wavelength limit (as expected). For $2\pi a_{\rm eff}/\lambda \gtrsim 1$, the fractional errors oscillate but are typically below 10%. The oscillatory errors will be suppressed for averages over size distributions.

Figures 3 and 4 are for porosity $\mathcal{P}=0$. In Appendix C, we show similar figures for astrodust grains with porosity $\mathcal{P}=0.5$, with $a_{\rm eff}=0.25~\mu{\rm m}$ to keep the peak in $C_{\rm pol}$ near $0.55~\mu{\rm m}$. The peak normalized extinction cross sections are only slightly reduced, but the polarizing efficiencies are lowered by about a factor of 2 relative to the results for $\mathcal{P}=0$. The MFPA is seen to provide a good approximation to the orientation-averaged cross sections for $\mathcal{P}=0.5$, just as for $\mathcal{P}=0$.

5. Starlight Polarization Efficiency Integral Φ

For each α , ψ , and magnetic field orientation γ , we define a dimensionless starlight polarization efficiency integral

$$\Phi(a_{\text{eff}}, b/a, \gamma, \alpha, \psi) = \frac{1}{f_{\text{align}}(a_{\text{eff}})\sin^2\gamma} \int_{\lambda_1}^{\lambda_2} \frac{1}{2} \frac{\langle C_{\text{ext},y} \rangle - \langle C_{\text{ext},x} \rangle}{V} d\lambda, \quad (27)$$

where $f_{\rm align}$ is given by Equation (5), $V \equiv (4\pi/3)a_{\rm eff}^3$ is the grain volume, and $\langle C_{\rm ext,y} \rangle$ and $\langle C_{\rm ext,x} \rangle$ are orientational

averages calculated from Equations (A10) and (A11). We set $\lambda_1 = 0.15$ and $\lambda_2 = 2.5 \ \mu m$. The methodology used here is insensitive to the exact choice of λ_1 and λ_2 , provided only that $[\lambda_1, \ \lambda_2]$ include the wavelength range $0.25-1.2 \ \mu m$ where starlight polarization is observed to be strong.

Figure 5 shows Φ calculated for different grain shapes for various orientation distributions (three values of γ and three values of ψ) for grains with perfect internal alignment ($\alpha=0$ for oblate, $\alpha=\pi/2$ for prolate). We show Φ for grain sizes that contribute strongly to the observed starlight polarization ($a_{\rm eff}=0.15~\mu{\rm m}$ for ${\cal P}=0$, $a_{\rm eff}=0.25~\mu{\rm m}$ for ${\cal P}=0.5$). Figure 5 shows that Φ depends strongly on the grain shape b/a but is almost independent of both γ and the alignment angle ψ .

If the MPFA is a good approximation (i.e., if $\frac{1}{2}\langle C_{\text{ext},y} - C_{\text{ext},x} \rangle \approx C_{\text{pol}}(\lambda) f_{\text{align}} \sin^2 \gamma$), then

$$\Phi(a_{\rm eff}, b/a, \gamma, \alpha, \psi) \approx \Phi^{\rm MPFA}(a_{\rm eff}, b/a),$$
 (28)

where

$$\Phi^{\text{MPFA}} \equiv \int_{\lambda_{l}}^{\lambda_{2}} \frac{C_{\text{pol}}(b/a, a_{\text{eff}}, \lambda)}{V} d\lambda$$

$$\equiv \int_{\lambda_{l}}^{\lambda_{2}} \frac{3}{4} \frac{Q_{\text{pol}}(b/a, a_{\text{eff}}, \lambda)}{a_{\text{eff}}} d\lambda, \tag{29}$$

where $C_{\rm pol}$ is defined in Equation (19). We have calculated Φ for astrodust grains; $\Phi_{\rm Ad}$ is plotted versus b/a in Figure 5, together with $\Phi_{\rm Ad}^{\rm MPFA}$. The upper panels of Figure 5 show the fractional difference between $\Phi_{\rm Ad}$ and $\Phi_{\rm Ad}^{\rm MPFA}$ for different

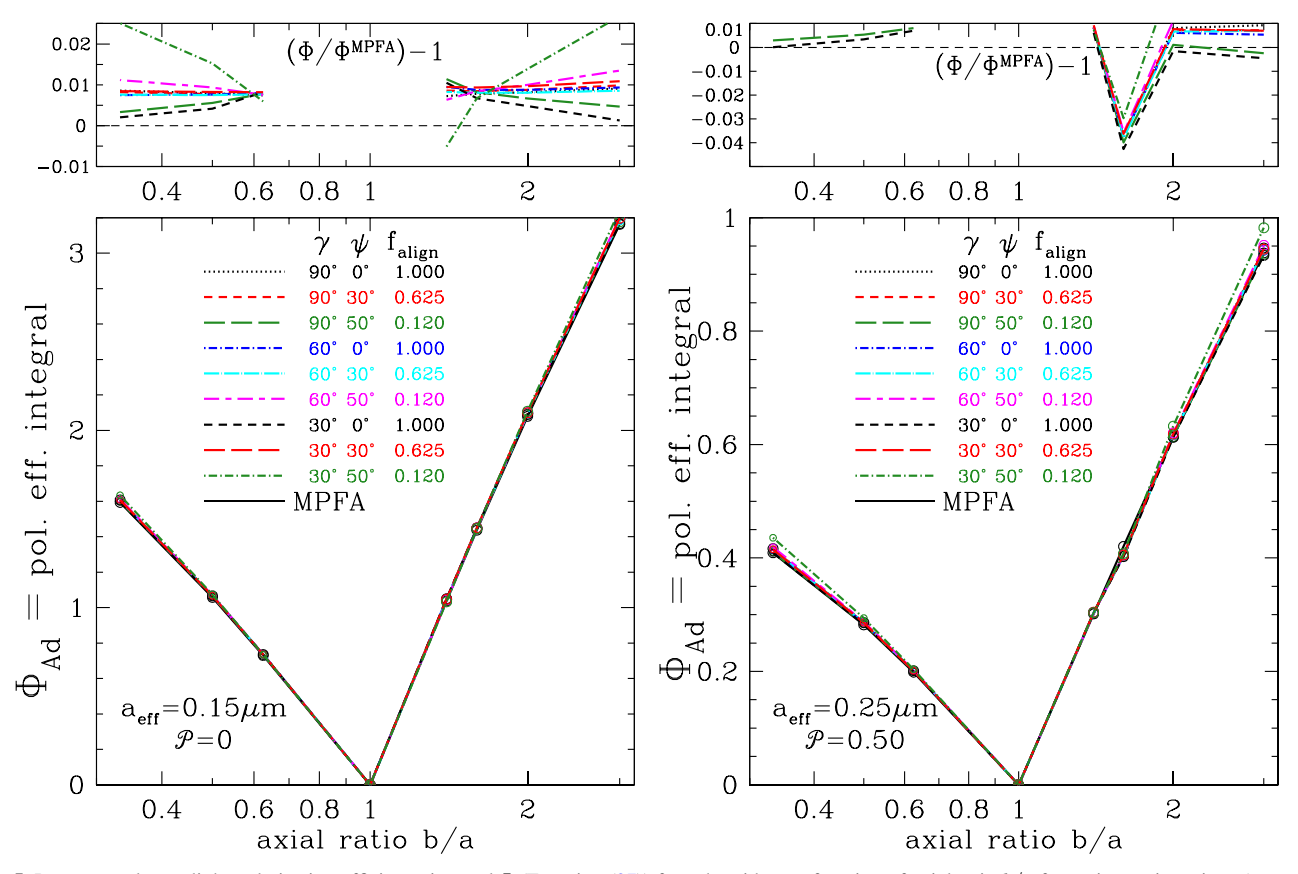


Figure 5. Lower panels: starlight polarization efficiency integral Φ (Equation (27)) for spheroids as a function of axial ratio b/a for various orientations (see text) for $\lambda_1=0.15~\mu\text{m},~\lambda_2=2.5~\mu\text{m}$. Here γ is the angle between $\textbf{\textit{B}}_0$ and the line of sight; ψ is the angle between ω and ω 0, with ω 0 precessing around ω 0. Grains are "astrodust" (see text) with porosity ω 1 or (left) and 0.5 (right). ω 2 is nearly independent of both ω 3 and the degree of alignment; thus, the MPFA is an excellent approximation. Upper panels: fractional error (ω 4/ ω 4/MPFA) – 1 for different values of ω 4 and ω 7. The MPFA is generally accurate to within a few percent.

alignment cases. We see that Φ^{MPFA} approximates the actual Φ to within a few percent. We conclude that the MPFA is an excellent approximation for computing the polarization efficiency integral for partially aligned spinning grains. Thus, for purposes of discussing the polarization efficiency integral Φ , we do not need to average $C_{\mathrm{ext},x}$ and $C_{\mathrm{ext},y}$ over the actual distribution of grain orientations; we can simply take $\Phi \approx \Phi^{\mathrm{MPFA}}$.

 $\Phi^{\mathrm{MPFA}}(a_{\mathrm{eff}},b/a)$ is a measure of the polarizing efficiency for grains of a specified size, shape, and porosity. We will show below how the observed starlight polarization can be used to constrain Φ^{MPFA} , thereby constraining the properties of the grains responsible for polarization of starlight.

6. Starlight Polarization Integral Π_{obs}

Models to reproduce the extinction and polarization require specifying the shape of the grains, the grain size distribution $dn_{\rm gr}/da_{\rm eff}$, and $f_{\rm align}(a_{\rm eff})$, the fractional alignment of grains of size $a_{\rm eff}$ with the local magnetic field direction (see Equation (5)). Suppose the grains to be spheroids with axial ratio b/a. Using the MPFA (Equation (24)), the polarization is

$$p(\lambda) \approx N_{\rm H} \int da_{\rm eff} \left(\frac{1}{n_{\rm H}} \frac{dn_{\rm gr}}{da_{\rm eff}}\right) C_{\rm pol}(b/a, a_{\rm eff}, \lambda) f_{\rm align}(a_{\rm eff}) \sin^2 \gamma,$$
(30)

where $N_{\rm H}$ is the column density of H nucleons on the sightline.

The strength and wavelength dependence of starlight polarization have been measured on many sightlines (e.g., Serkowski et al. 1975; Bagnulo et al. 2017). The observed wavelength dependence of the polarization is quite well described by the empirical fitting function found by Serkowski (1973),

$$p(\lambda) \approx p_{\text{max}} \exp\left[-K(\ln(\lambda/\lambda_{\text{p}}))^2\right].$$
 (31)

Equation (31), referred to as the "Serkowski law," provides a good empirical description of observed starlight polarization from $2.2 \,\mu\text{m}$ (Whittet et al. 1992) to wavelengths as short as $0.15 \,\mu\text{m}$ (Martin et al. 1999).

Serkowski et al. (1975) suggested $\lambda_{\rm p} \approx 0.55 \,\mu{\rm m}$ and $K \approx 1.15$ as typical. Sightline–to–sightline variations in both $\lambda_{\rm p}$ and K are seen and found to be correlated. Whittet et al. (1992) found

$$K \approx 0.01 + 1.66(\lambda_{\rm p}/\mu{\rm m}),$$
 (32)

although Bagnulo et al. (2017) reported deviations from this relation. Martin et al. (1999) showed that an improved fit to the visible-UV polarization is obtained with

$$K \approx -0.59 + 2.56(\lambda_{\rm p}/\mu{\rm m}).$$
 (33)

As a compromise between the UV and IR, Whittet (2003) recommended

$$K \approx -0.29 + 2.11(\lambda_{\rm p}/\mu{\rm m}).$$
 (34)

$\frac{\lambda_{\rm p}}{(\mu {\rm m})}$	K	$\Pi_{ m obs}/p_{ m max} \ (\mu{ m m})$	$\sigma_{ m obs}$	Reference
0.55	1.15	1.07	0.73	Serkowski et al. (1975)
0.45	0.76	1.13	0.65	Whittet et al. (1992)
0.50	0.84	1.17	0.64	**
0.55	0.92	1.20	0.63	**
0.60	1.01	1.23	0.62	,,
0.65	1.09	1.25	0.64	"
0.45	0.56	1.32	0.69	Martin et al. (1999)
0.50	0.69	1.29	0.62	,,
0.55	0.82	1.27	0.63	,,
0.60	0.95	1.26	0.63	**
0.65	1.07	1.27	0.62	"
0.45	0.66	1.22	0.67	Whittet (2003)
0.50	0.77	1.22	0.65	**
0.55	0.87	1.23	0.64	**
0.60	0.98	1.25	0.62	,,
0.65	1.08	1.26	0.61	"
0.55	0.87	1.23	0.64	Representative

Note. ^a for $\lambda_1 = 0.15$, $\lambda_2 = 2.5 \ \mu \text{m}$

At longer wavelengths (e.g., 3.5 and 4.8 μ m), the Serkowski law (Equation (31)) appears to underestimate the polarization, and a power-law dependence has been suggested (Martin & Whittet 1990); at even longer wavelengths, there is a prominent polarization feature near 10 μ m produced by the Si-O absorption resonance in silicates (Dyck et al. 1973; Smith et al. 2000). However, the Serkowski law (Equation (31)) provides a generally good fit to the observed polarization from the shortest observed UV wavelengths to the near-infrared (see discussion in Hensley & Draine 2021), and we will use it here between 0.15 and 2.5 μ m. We will consider $\lambda_p = 0.55 \mu$ m and K = 0.87 as a representative example (see bold entries Table 1).

We will see below that the starlight polarization integrated over wavelength provides a very useful constraint on the population of aligned grains. We define the observed starlight polarization integral for a sightline

$$\Pi_{\text{obs}} \equiv \int_{\lambda_1}^{\lambda_2} p(\lambda) d\lambda, \tag{35}$$

with λ_1 and λ_2 chosen to capture the polarization peak: $\lambda_1 \lesssim \lambda_p/2$ and $\lambda_2 \gtrsim 2\lambda_p$. If the observed polarization is approximated by the Serkowski law (Equation (31)), the polarization integral becomes

$$\Pi_{\text{obs}} \approx p_{\text{max}} \times \lambda_{\text{p}} \frac{\sqrt{\pi} e^{1/4K}}{2\sqrt{K}} [\text{erf}(s_1) + \text{erf}(s_2)],$$
 (36)

$$s_1 \equiv \sqrt{K} \left[\ln(\lambda_p/\lambda_l) + \frac{1}{2K} \right],$$
 (37)

$$s_2 \equiv \sqrt{K} \left[\ln(\lambda_2/\lambda_p) - \frac{1}{2K} \right], \tag{38}$$

where erf(s) $\equiv (2/\sqrt{\pi}) \int_0^s e^{-x^2} dx$ is the usual error function. We set $\lambda_1 = 0.15$ and $\lambda_2 = 2.5 \,\mu\text{m}$, so that we only use the Serkowski law at wavelengths where it has been confirmed to be applicable.

Values of $\Pi_{\rm obs}/p_{\rm max}$ are given in Table 1 for various $\lambda_{\rm p}$ and K. It is noteworthy that $\Pi_{\rm obs}/p_{\rm max}$ is not very sensitive to the precise values of $\lambda_{\rm p}$ and K. We take $\Pi_{\rm obs}/p_{\rm max} \approx 1.23~\mu{\rm m}$ as a representative value for the diffuse ISM.

7. Characteristic Size of the Aligned Grains

The dust in the ISM must have shapes and sizes such that the population of aligned grains reproduces the Serkowski law (Equation (31)); this requires a distribution of grain sizes, but the most important grains will be the ones contributing to the polarization at wavelengths near the peak at $\lambda_{\rm p}\approx 0.55~\mu{\rm m}.$

We define an effective wavelength $\lambda_{\rm p,eff}(a_{\rm eff}, b/a)$ for the polarization contribution by grains of a given size $a_{\rm eff}$ and shape b/a:

$$\lambda_{\text{p,eff}} \equiv \exp\left[\frac{\int_{\lambda_{\text{l}}}^{\lambda_{2}} (\ln \lambda) C_{\text{pol}}(b/a, a_{\text{eff}}, \lambda) d \ln \lambda}{\int_{\lambda_{\text{l}}}^{\lambda_{2}} C_{\text{pol}}(b/a, a_{\text{eff}}, \lambda) d \ln \lambda}\right]. \tag{39}$$

We can also calculate the effective wavelength $\lambda_{p,eff}^{obs}$ for the Serkowski law (Equation (31)):

$$\ln(\lambda_{\rm p,eff}^{\rm obs}) \equiv \frac{\int_{\lambda_{\rm l}}^{\lambda_{\rm 2}} (\ln \lambda) p(\lambda) d \ln \lambda}{\int_{\lambda_{\rm l}}^{\lambda_{\rm 2}} p(\lambda) d \ln \lambda}$$
(40)

$$=\ln(\lambda_{\rm p}) + \frac{1}{\sqrt{\pi K}} \frac{\exp[-K(\ln(\lambda_{\rm p}/\lambda_{\rm l}))^2] - \exp[-K(\ln(\lambda_{\rm 2}/\lambda_{\rm p}))^2]}{\exp[\sqrt{K}\ln(\lambda_{\rm p}/\lambda_{\rm l})] + \exp[\sqrt{K}\ln(\lambda_{\rm 2}/\lambda_{\rm p})]},$$
(41)

For $\lambda_{\rm p}=0.55~\mu{\rm m}$, $K=0.87,~\lambda_1=0.15~\mu{\rm m}$, and $\lambda_2=2.5~\mu{\rm m}$, we have

$$\lambda_{\text{p,eff}}^{\text{obs}} = 0.567 \ \mu\text{m}. \tag{42}$$

Thus, the grains that dominate the starlight polarization should have sizes $a_{\rm eff}$ such that $\lambda_{\rm p,eff} \approx 0.57~\mu{\rm m}$. $C_{\rm pol}^{\rm MPFA}(\lambda)$ and $\lambda_{\rm p,eff}$ depend on the adopted dielectric

 $C_{\rm pol}^{\rm MPFA}(\lambda)$ and $\lambda_{\rm p,eff}$ depend on the adopted dielectric function and grain size and shape. Figure 6 shows $\lambda_{\rm p,eff}$ as a function of $a_{\rm eff}$ for astrodust grains with porosity $\mathcal{P}=0$ and 0.5. The observed polarization, peaking near $\lambda_{\rm p}\approx 0.55~\mu{\rm m}$, is dominated by grains with sizes $a_{\rm eff}$ close to a characteristic grain size $a_{\rm char}$, defined to be the size for which $\lambda_{\rm p,eff}(a)\approx \lambda_{\rm p,eff}^{\rm obs}=0.567~\mu{\rm m}$. We see that $a_{\rm char}\approx 0.15~\mu{\rm m}$ for $\mathcal{P}=0$, and $a_{\rm char}\approx 0.24~\mu{\rm m}$ if the porosity $\mathcal{P}\approx 0.5$. Figure 7 shows how $a_{\rm char}$ depends on \mathcal{P} ; the numerical results are approximated by the simple fitting function

$$a_{\text{char}} \approx \frac{0.152 \ \mu\text{m}}{(1 - \mathcal{P})^{2/3}}.$$
 (43)

8. Polarization Profile Width

For each grain size $a_{\rm eff}$ and shape b/a, we define a measure of the width of the polarization profile $C_{\rm pol}(\lambda)$,

$$\sigma(a_{\text{eff}}, b/a) \equiv \frac{\int_{\lambda_{l}}^{\lambda_{2}} d \ln \lambda [\ln(\lambda) - \ln(\lambda_{\text{p,eff}})]^{2} C_{\text{pol}}(\lambda)}{\int_{\lambda_{l}}^{\lambda_{2}} d \ln \lambda C_{\text{pol}}(\lambda)}, (44)$$

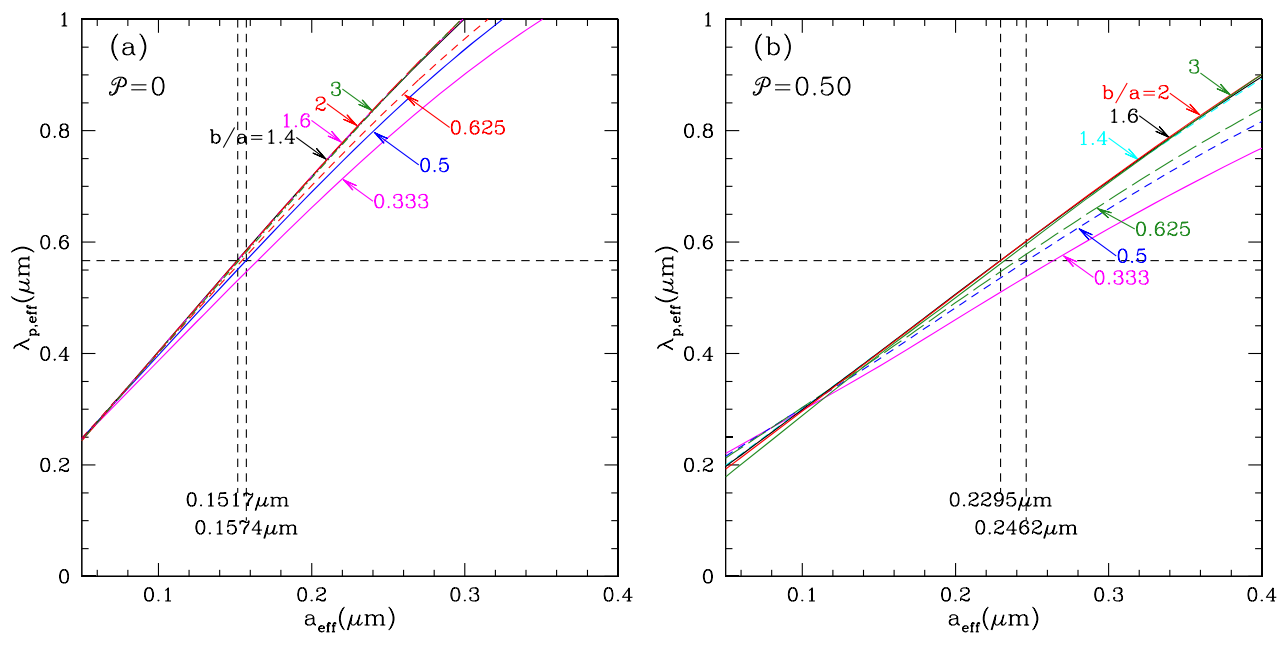


Figure 6. Effective wavelength $\lambda_{\rm p,eff}$ for polarization (Equation (39)) as a function of $a_{\rm eff}$ for different axial ratios. (a) Astrodust grains with no porosity. (b) Astrodust grains with porosity $\mathcal{P}=0.5$ The horizontal dashed line shows $\lambda_{\rm p,eff}=0.567~\mu{\rm m}$ for the Serkowski law with $\lambda_{\rm p}=0.55~\mu{\rm m}$ and K=0.87. In each panel, the vertical lines show the values of $a_{\rm eff}$ corresponding to $\lambda_{\rm p,eff}=0.567~\mu{\rm m}$ for astrodust with b/a=0.5 and 2. Porous grains have to be larger than nonporous grains to have $\lambda_{\rm p,eff}=0.567~\mu{\rm m}$.

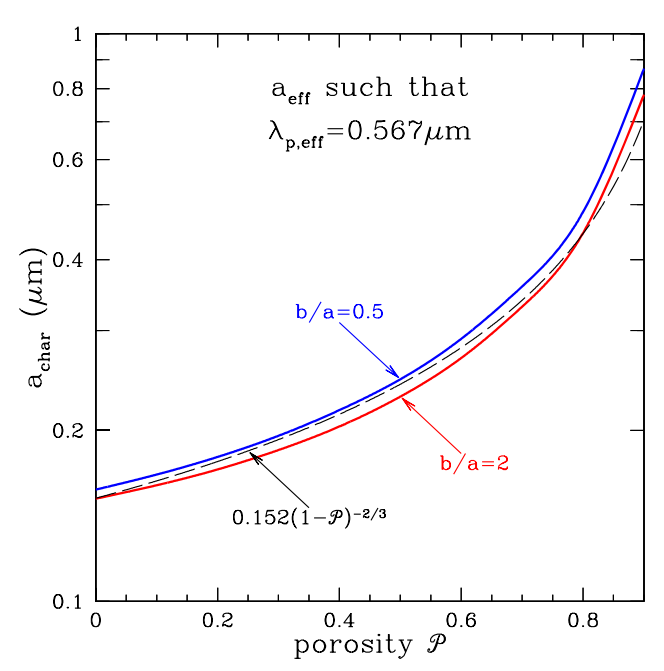


Figure 7. Characteristic grain size $a_{\rm char}$ such that $\lambda_{\rm p,eff}=0.567~\mu{\rm m}$ as a function of porosity ${\cal P}$ for oblate (b/a=2) and prolate (b/a=0.5) spheroids. Also shown (dashed curve) is the fitting function $a_{\rm char}=0.152~\mu{\rm m}(1-{\cal P})^{-2/3}$.

where $\lambda_{\rm p,eff}$ is given by Equation (39). Calculated values of σ for different axial ratios b/a are shown in Figures 8(a) and (b) for porosities $\mathcal{P}=0$ and 0.5. Prolate shapes have higher values of σ (broader profiles) than oblate shapes, as was already noticeable for the selected sizes shown in Figures 2 and 3. For the prolate shapes, σ also increases significantly with increasing porosity, as seen by comparing Figures 8(a) and (b).

The observed interstellar polarization has a characteristic width determined by the parameter K in the Serkowski fitting function (Equation (31)). We calculate the "observed" σ :

$$\sigma_{\text{obs}} = \frac{\int_{\lambda_{l}}^{\lambda_{2}} d \ln \lambda \left[\ln(\lambda) - \ln(\lambda_{\text{p,eff}}^{\text{obs}})\right]^{2} \exp\left[-K(\ln(\lambda/\lambda_{p}))^{2}\right]}{\int_{\lambda_{l}}^{\lambda_{2}} d \ln \lambda \exp\left[-K(\ln(\lambda/\lambda_{p}))^{2}\right]}.$$
(45)

For the values of K and λ_p from Whittet (2003) listed in Table 1, we find $\sigma_{\rm obs} = 0.64 \pm 0.03$ (shaded area in Figure 8).

The observed polarization of starlight is produced by a size distribution of aligned grains, with sizes $0.1 \, \mu \text{m} \lesssim a_{\text{eff}} \lesssim 0.3 \, \mu \text{m}$ (Kim & Martin 1995; Draine & Fraisse 2009; Siebenmorgen et al. 2014; Fanciullo et al. 2017; Guillet et al. 2018). If the aligned grains have a distribution of sizes, σ for the mixture will be larger than for a single size, because $\lambda_{\text{p,eff}} \propto a_{\text{eff}}$ (see Figure 6). Thus, we expect the single-size $\sigma(a_{\text{eff}}, b/a)$ to be significantly smaller than σ_{obs} .

For $\mathcal{P}=0$ and oblate shapes, the σ for individual grains is significantly smaller than $\sigma_{\rm obs}$ (see Figure 8), so that a size distribution for the aligned grains may be consistent with $\sigma_{\rm obs}$. For prolate shapes, this is more difficult, because the individual shapes already have σ values approaching $\sigma_{\rm obs}$; this is especially pronounced for $\mathcal{P}=0.5$. For porous grains, the size distributions needed to explain the wavelength dependence of the extinction will likely result in a polarization profile with $\sigma > \sigma_{\rm obs}$, especially for prolate shapes. (Although we note that Guillet et al. 2018 were able to fit the starlight polarization with a model that included 3:1 prolate spheroids.)

This is one argument favoring oblate versus prolate shapes for interstellar grains. As we will see below, the strength of the starlight polarization also favors oblate shapes.

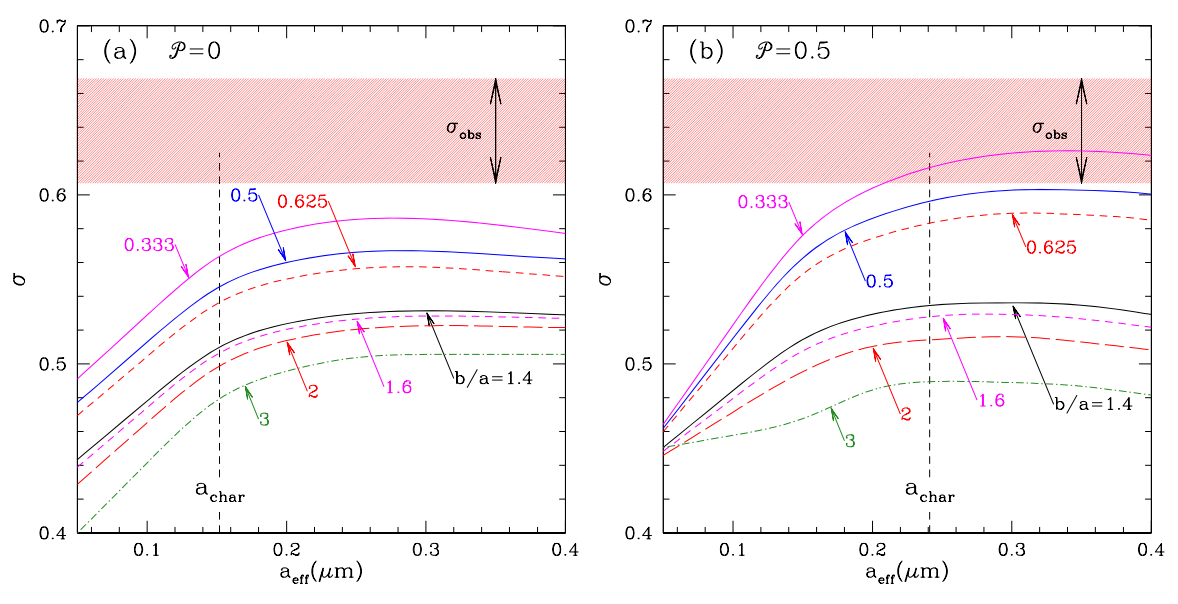


Figure 8. Fractional width of the polarization profile for individual grains, as measured by σ . Results are shown for seven different values of b/a and for porosities $\mathcal{P}=0$ and 0.5. The shaded area shows the range of the fractional width $\sigma_{\rm obs}$ for the observed starlight polarization (see text). Since grains with a range of sizes contribute to the observed polarization, the values of σ for the contributing sizes must be smaller than the overall width $\sigma_{\rm obs}$.

9. Φ , Aligned Mass Fraction $\langle f_{\rm align} \rangle$, and Limits on Axial Ratios

Observations of starlight polarization (Serkowski et al. 1975; Bagnulo et al. 2017) found

$$p_{\text{max}} \lesssim 0.090 \frac{E(B-V)}{\text{mag}} \tag{46}$$

for the sightlines that have been sampled; given that $\lesssim 10^2$ sightlines had accurate measurements of $p_{\rm max}/E(B-V)$, some sightlines may exceed the limit in Equation (46). From observations of polarized submillimeter emission, Planck Collaboration XII. (2020) recommended

$$p_{\text{max}} \lesssim 0.130 \frac{E(B-V)}{\text{mag}} \tag{47}$$

as a more realistic estimate of the upper limit, and Panopoulou et al. (2019) found sightlines with $p_{\rm max}\approx 0.13E(B-V)/{\rm mag}$. It is reasonable to suppose that the highest values of $p_{\rm max}/E(B-V)$ correspond to sightlines where $\sin^2\!\gamma\approx 1$. Thus, we take

$$p_{\text{max}} \approx 0.130 \sin^2 \gamma \, \frac{E(B-V)}{\text{mag}}.\tag{48}$$

Models to reproduce the observed wavelength-dependent extinction typically have grain mass distributions peaking around $a_{\rm eff}\approx 0.25~\mu{\rm m}$ but with appreciable mass in the $a\lesssim 0.1~\mu{\rm m}$ grains that are required to reproduce the observed rapid rise in extinction into the UV. The classic MRN model (Mathis et al. 1977) reproduces the extinction using spherical grains with $dn/da \propto a^{-3.5}$ for $0.005~\mu{\rm m} \leqslant a \leqslant 0.25~\mu{\rm m}$; this distribution has 45% of the grain mass in grains with $a<0.07~\mu{\rm m}$. More recent grain models with more complicated size distributions (e.g., Weingartner & Draine 2001; Zubko et al. 2004) have similar fractions of the silicate mass in grain sizes $a_{\rm eff}<0.07~\mu{\rm m}$. However, models to reproduce the

polarization of starlight (e.g., Kim & Martin 1995; Draine & Fraisse 2009; Siebenmorgen et al. 2014; Fanciullo et al. 2017; Guillet et al. 2018, B. S. Hensley & B. T. Draine 2021, in preparation) require that grains smaller than $\lesssim 0.07~\mu m$ have minimal alignment; if these grains were aligned, the polarization would exceed the observed low polarization in the UV (Martin et al. 1999). If we estimate > 30% of the dust mass to be in grains that are not aligned, then the mass-averaged alignment efficiency

$$\langle f_{\text{align}} \rangle < 0.70.$$
 (49)

Figure 9 (lower panels) shows the starlight polarization efficiency integral $\Phi_{\rm Ad}^{\rm MPFA}$ calculated for astrodust grains as a function of axial ratio b/a for selected sizes $a_{\rm eff}$, for three cases: zero porosity ($\mathcal{P}=0$), moderate porosity ($\mathcal{P}=0.30$), and high porosity ($\mathcal{P}=0.50$). Increasing porosity results in a significant decrease in $\Phi_{\rm Ad}^{\rm MPFA}$ because, per unit volume, the more porous grains are less effective polarizers.

For the grain sizes required to reproduce the observed polarization of starlight, the starlight polarization efficiency factor $\Phi_{\rm Ad}^{\rm MPFA}(b/a,\,a_{\rm eff})$ is seen to be almost independent of $a_{\rm eff}$. The curves in Figure 9 are for $a_{\rm eff}=a_{\rm char}$, with $a_{\rm char}$ from Equation (43).

For an assumed grain shape, the total volume of the aligned grains can be estimated from the (observed) starlight polarization integral $\Pi_{\rm obs}$ and the (theoretical) polarization efficiency integral $\Phi(b/a)$ without the need to solve for the actual size distribution of the aligned grains. Integrating Equation (30) over wavelength, we obtain

$$\Pi_{\text{obs}} = N_{\text{H}} \int da_{\text{eff}} \left(\frac{1}{n_{\text{H}}} \frac{dn_{\text{gr}}}{da_{\text{eff}}} \right) \frac{4}{3} \pi a_{\text{eff}}^3 \Phi(b/a, a_{\text{eff}}) f_{\text{align}}(a_{\text{eff}}) \sin^2 \gamma$$
(50)

$$\approx N_{\rm H} \Phi(b/a, a_{\rm char}) \sin^2 \gamma \int da_{\rm eff} \left(\frac{1}{n_{\rm H}} \frac{dn_{\rm gr}}{da_{\rm eff}} \right) \frac{4}{3} \pi a_{\rm eff}^3 f_{\rm align}(a_{\rm eff}), \tag{51}$$

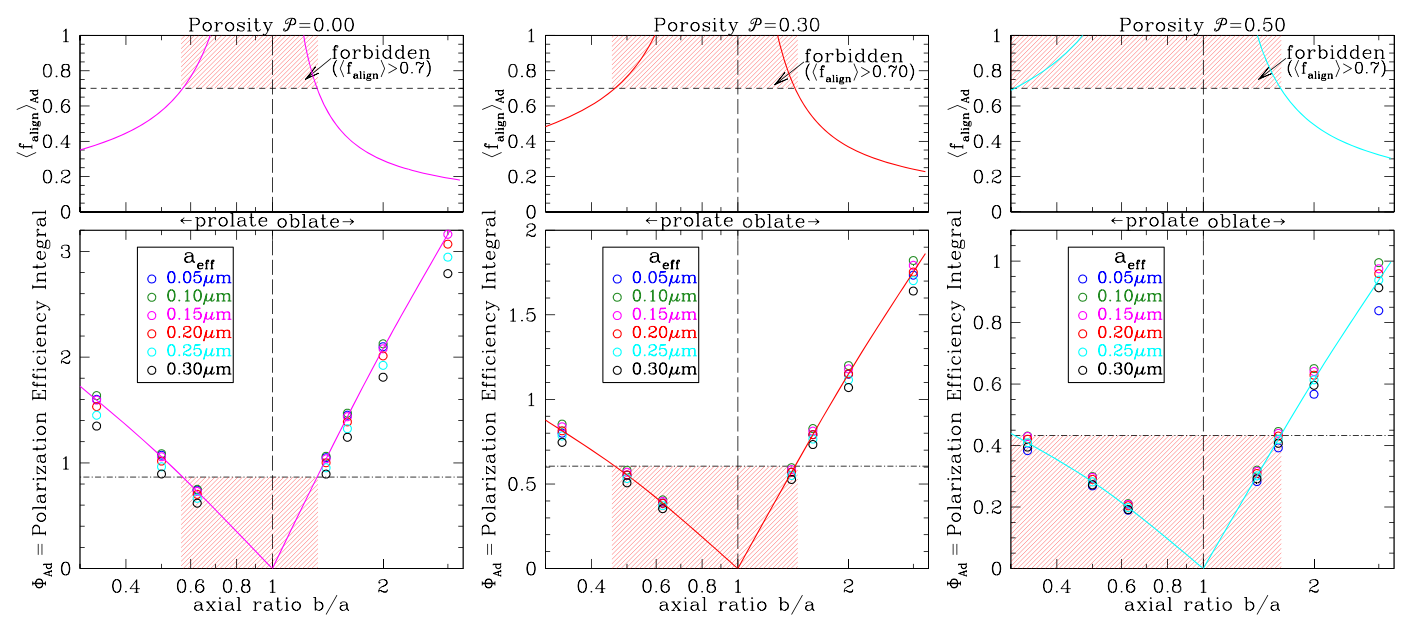


Figure 9. Lower panels: starlight polarization efficiency integral $\Phi_{\rm Ad}^{\rm MPFA}$ for "astrodust" spheroids as a function of axial ratio b/a for six grain sizes and three different porosities \mathcal{P} . Upper panels: $\langle f_{\rm align} \rangle$, the aligned mass fraction of the astrodust grains. Values of $\langle f_{\rm align} \rangle > 0.7$ are forbidden (shaded regions). The trend lines shown in each panel are for the grain size closest to $a_{\rm char} = 0.152~\mu {\rm m}/(1-\mathcal{P})^{2/3}$ (see Figure 7 and Equation (43)) and are correspondingly color-coded.

where in Equation (51) we take $\Phi(a_{\rm eff})$ to be approximately constant for grain sizes $a_{\rm eff}$ near the characteristic grain size $a_{\rm char}$. Let $V_{\rm align}$ be the volume per H of aligned grains:

$$V_{\text{align}} \equiv \int da_{\text{eff}} \left(\frac{1}{n_{\text{H}}} \frac{dn_{\text{gr}}}{da_{\text{eff}}} \right) \frac{4}{3} \pi a_{\text{eff}}^3 f_{\text{align}}(a_{\text{eff}}), \tag{52}$$

Equation (51) becomes

$$\Pi_{\rm obs} \approx N_{\rm H} \, \Phi(b/a, \, a_{\rm char}) \, \sin^2 \gamma \, V_{\rm align}.$$
 (53)

We use the observational results

$$N_{\rm H}/E(B-V) \approx 8.8 \times 10^{21} \,\rm cm^{-2} mag^{-1}$$
 (54)

(Lenz et al. 2017), $p_{\rm max}/E(B-V)\approx 0.130\,{\rm sin^2}\,\gamma\,{\rm mag^{-1}}$ (Equation (48)), and $\Pi_{\rm obs}/p_{\rm max}=1.23~\mu{\rm m}$ (see Table 1). For a given assumed grain shape b/a and an approximate estimate for the characteristic size $a_{\rm char}$, we can now estimate the volume of aligned dust per H nucleon without needing to solve for the size distribution of the aligned grains:

$$V_{\text{align}} \approx \frac{p_{\text{max}} / E(B - V)}{N_{\text{H}} / E(B - V)} \times \frac{\Pi_{\text{obs}} / p_{\text{max}}}{\Phi(b / a, a_{\text{char}})}$$
$$\approx \frac{1.82 \times 10^{-27} \text{ cm}^{3} \text{H}^{-1}}{\Phi^{\text{MPFA}}(b / a, a_{\text{char}})}, \tag{55}$$

for the representative case $\lambda_{\rm p} = 0.55\,\mu{\rm m}$ and K = 0.87 (see Table 1). For comparison, the total volume of astrodust grains per H nucleon in the diffuse high-latitude ISM is estimated to be

$$V_{\rm Ad} = 3.0 \times 10^{-27} (1 - \mathcal{P})^{-1} \,\mathrm{cm}^3 \mathrm{H}^{-1}$$
 (56)

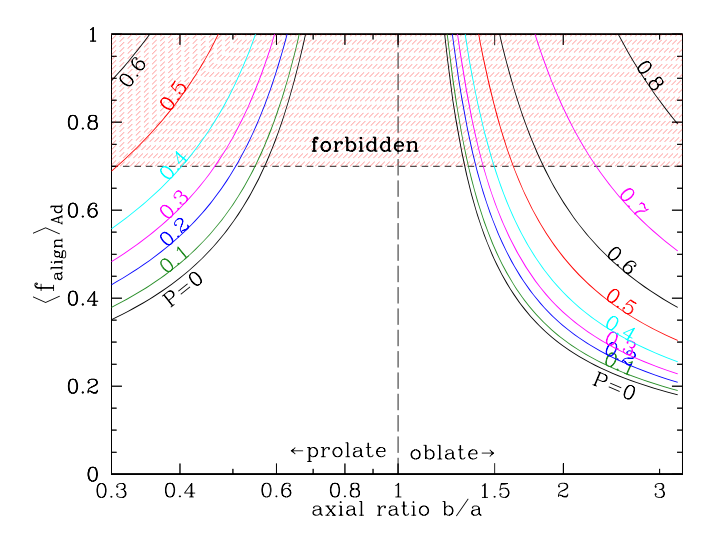


Figure 10. Mass-weighted aligned fraction of astrodust grains, $\langle f_{\rm align} \rangle$ (see Equation (57)), as a function of axial ratio b/a. The region $\langle f_{\rm align} \rangle \gtrsim 0.7$ (shaded in red) is forbidden by low levels of polarization in the ultraviolet (see text).

(Draine & Hensley 2021). The mass-weighted alignment efficiency is then

$$\langle f_{\rm align} \rangle_{\rm Ad} \equiv \frac{V_{\rm align,Ad}}{V_{\rm Ad}} \approx \frac{0.61(1-\mathcal{P})}{\Phi_{\rm Ad}^{\rm MPFA}(b/a,\,a_{\rm char})}.$$
 (57)

The upper panels in Figure 9 show the $\langle f_{\rm align} \rangle_{\rm Ad}$ required to account for the observed polarization of starlight on sightlines with the largest $p_{\rm max}/E(B-V)$ (see Equation (57)). The shaded regions in Figure 9 correspond to $\langle f_{\rm align} \rangle_{\rm Ad} > 0.7$, which is forbidden (see Equation (49)). For $\mathcal{P}=0$, Figure 9 shows that Equation (49) requires prolate grains to have axial ratios a/V

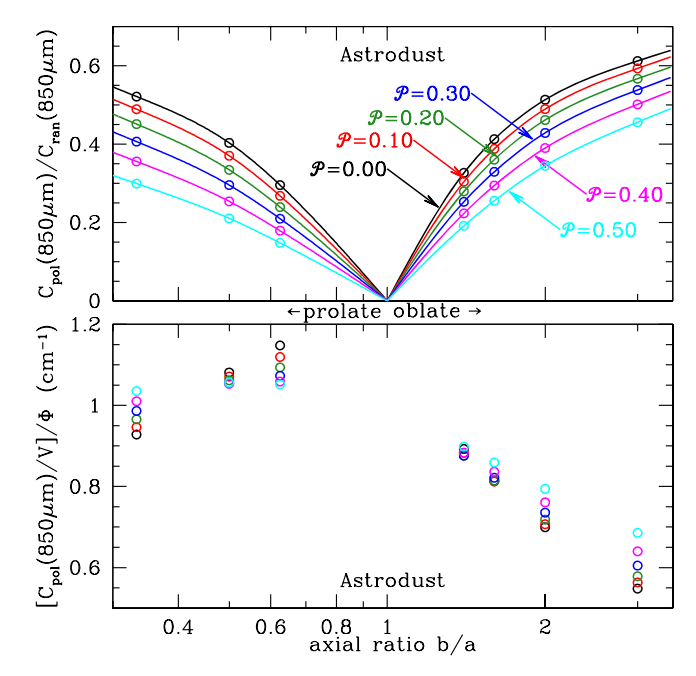


Figure 11. Upper panel: ratio of submillimeter ($\lambda = 850~\mu m$) polarization cross section to absorption cross section for astrodust spheroids as a function of axial ratio b/a. Lower panel: ratio of submillimeter polarization cross section per volume $C_{\text{pol,ext}}/V$ divided by starlight polarization efficiency factor Φ for astrodust grains as a function of axial ratio b/a. This measures the ability to polarize in the submillimeter relative to the optical.

 $b\gtrsim 1.8$ and oblate grains to have axial ratios $b/a\gtrsim 1.35$; less extreme axial ratios would not produce sufficient starlight polarization to reproduce observations, even with 70% of the dust mass perfectly aligned. For larger porosities ($\mathcal{P}=0.3$ and 0.5), Figure 9 shows that more extreme axial ratios are required, because porous grains are less efficient polarizers.

Figure 10 shows $\langle f_{\rm align} \rangle$ as a function of axial ratio b/a for selected porosities $\mathcal P$ from zero to 0.8. As expected, $\langle f_{\rm align} \rangle$ is a decreasing function of aspect ratio, because more extreme shapes are better polarizers.

If astrodust grains are porous, the total grain volume $V_{\rm Ad}$ is increased, and smaller values of $\Phi_{\rm Ad}$ are allowed. However, porous grains are less effective polarizers per unit mass, and the net effect is to require the astrodust grains to have more extreme axial ratios as ${\cal P}$ is increased; see Figure 10.

10. Polarized Submillimeter Emission

At submillimeter wavelengths, the electric dipole approximation is highly accurate. The aligned grains required to explain the polarization of starlight will generate submillimeter emission, with polarized intensity

$$\left(\frac{P_{\nu}}{N_{\rm H}}\right)_{\rm Ad} = V_{\rm align,Ad} \sin^2 \gamma \left(\frac{C_{\rm pol}(\nu)}{V}\right)_{\rm Ad} B_{\nu}(T_{\rm gr}), \tag{58}$$

where $B_{\nu}(T)$ is the usual Planck function, and $T_{\rm gr}$ is the dust temperature. With $V_{\rm align}$ constrained by Equation (55) so that astrodust material reproduces the starlight polarization, this

becomes

$$\left(\frac{P_{\nu}}{N_{\rm H}}\right)_{\rm Ad} = 1.82 \times 10^{-27} \,\mathrm{cm}^{3}\mathrm{H}^{-1}\mathrm{sin}^{2} \gamma$$

$$\times \frac{(C_{\rm pol}(\nu)/V)_{\rm Ad}}{\Phi_{\rm Ad}^{\rm MPFA}} \times B_{\nu}(T_{\rm gr}).$$
(59)

The ratio $(C_{\rm pol}(\nu)/V)_{\rm Ad}/\Phi_{\rm Ad}^{\rm MPFA}$ (see lower panel of Figure 11) determines the ratio of polarized emission per starlight polarization. This ratio depends on both axial ratio and porosity, and can therefore provide another constraint on b/a and ${\cal P}$. Prolate grains produce somewhat higher levels of polarized emission (per starlight polarization) than oblate grains.

According to Figure 11 (lower panel), $[C_{\rm pol}(850~\mu{\rm m})/V]/\Phi_{\rm Ad}^{\rm MPFA}$ depends on porosity ${\cal P}$ but more strongly on grain shape, with higher values for prolate shapes than for oblate shapes. The polarized infrared intensity per unit starlight polarization is (assuming $p_V \approx p_{\rm max}$)

$$\frac{P_{\nu}}{p_{V}} = \frac{\Pi_{\text{obs}}}{p_{\text{max}}} \times \frac{C_{\text{pol}}(\nu)/V}{\Phi} \times B_{\nu}(T_{\text{gr}})$$
 (60)

$$\left(\frac{P_{\nu}(850\mu\text{m})}{p_{V}}\right)_{\text{Ad}} \approx 7.99 \left(\frac{C_{\text{pol}}(850\mu\text{m})/V}{\text{cm}^{-1}}\right)_{\text{Ad}} \times \frac{1}{\Phi_{\text{Ad}}^{\text{MPFA}}} \left(\frac{1}{\exp(16.9 \text{ K}/T_{\text{gr}}) - 1}\right) \text{MJy sr}^{-1}.$$
(61)

Figure 12 shows $P_{\nu}(850 \ \mu\text{m})/p_{V}$ as a function of axial ratio b/a for six different porosities.

For intermediate Galactic latitudes, dust temperatures have been estimated to be $T_{\rm gr}=19.6$ (Planck Collaboration Int. XXII. 2015) and 19.4 K (Planck Collaboration Int. XLVIII. 2016). We show results for $T_{\rm gr}=19.5$ K, and also for $T_{\rm gr}=18.5$ and 20.5 K to show the sensitivity to the assumed dust temperature.

What is the actual value of $P_{\nu}(850 \, \mu\text{m})/p_{V}$? Planck Collaboration XII. (2020) found $P_{\nu}(850 \, \mu\text{m})/p_{V} = [5.42 \pm 0.05 \, \text{MJy sr}^{-1}]/1.11$ for 1505 stars, but a somewhat lower value, $[5.0 \, \text{MJy sr}^{-1}]/1.11$, for low column densities. Dust lying behind the star will raise P_{ν}/p_{V} , but Planck Collaboration XII. (2020) argued that this bias was negligible. A careful study of a small number of diffuse cloud sightlines using stars with Gaia distances placing them beyond the dust obtained a lower value, $P_{\nu}(850 \, \mu\text{m})/p_{V} = [4.2 \pm 0.1 \, \text{MJy sr}^{-1}]/1.11$ (Panopoulou et al. 2019, hereafter PHS19). For all of these cases, we apply a "color correction" factor of 1.11 to estimate monochromatic values at 353 GHz (see discussion in Hensley & Draine 2021). These values are shown in Figure 12. Why the PHS19 result differs from the Planck Collaboration XII. (2020) result is not clear.

Because of the uncertainty regarding the appropriate value of $P_{\nu}(850~\mu\text{m})/p_V$, we consider a dust model to be "allowed" if $P_{\nu}(850~\mu\text{m})/p_V$ falls anywhere in the range 3.69–4.93 MJy sr⁻¹ spanned by the Planck Collaboration XII. (2020) and PHS19 results, for some T_{dust} within the range 18.5–20.5 K. A number of our astrodust models fall within this range. The ones that also have $f_{\text{align}} < 0.7$ (i.e., outside the shaded red regions in

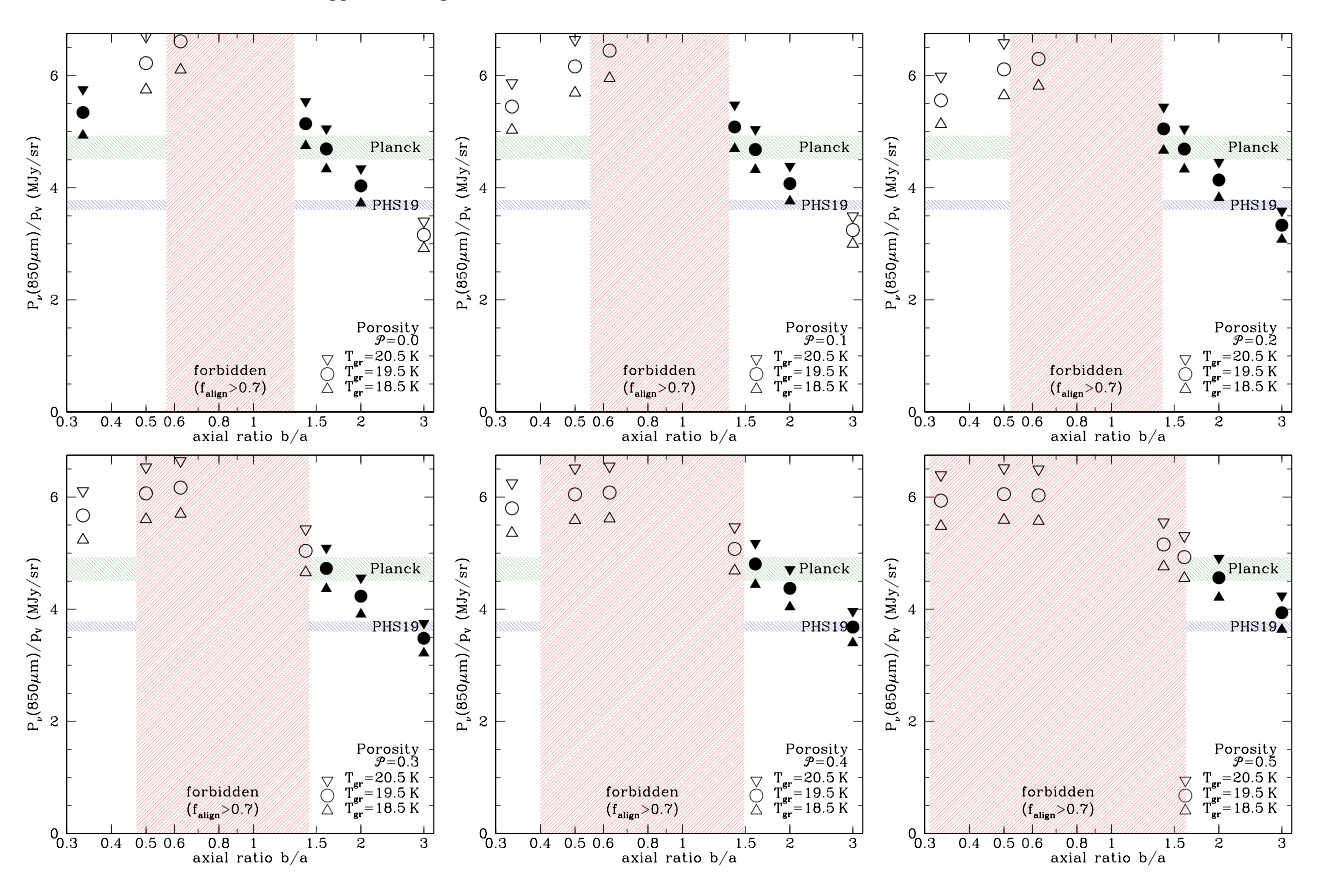


Figure 12. $P_{\nu}(850 \ \mu\text{m})/p_V$, the predicted monochromatic polarized 850 μ m intensity per unit V-band polarization fraction for astrodust with $T_{gr}=18.5$, 19.5, and 20.5 K for six porosities \mathcal{P} . Green shaded region: Planck results for diffuse clouds (Planck Collaboration XII. 2020) Blue shaded region: results of PHS19. Planck data have been color-corrected (see text). Red shaded region: axial ratios ruled out by $\langle f_{align} \rangle < 0.7$ (see Figure 10). Filled symbols: cases that may be compatible with observations (see text).

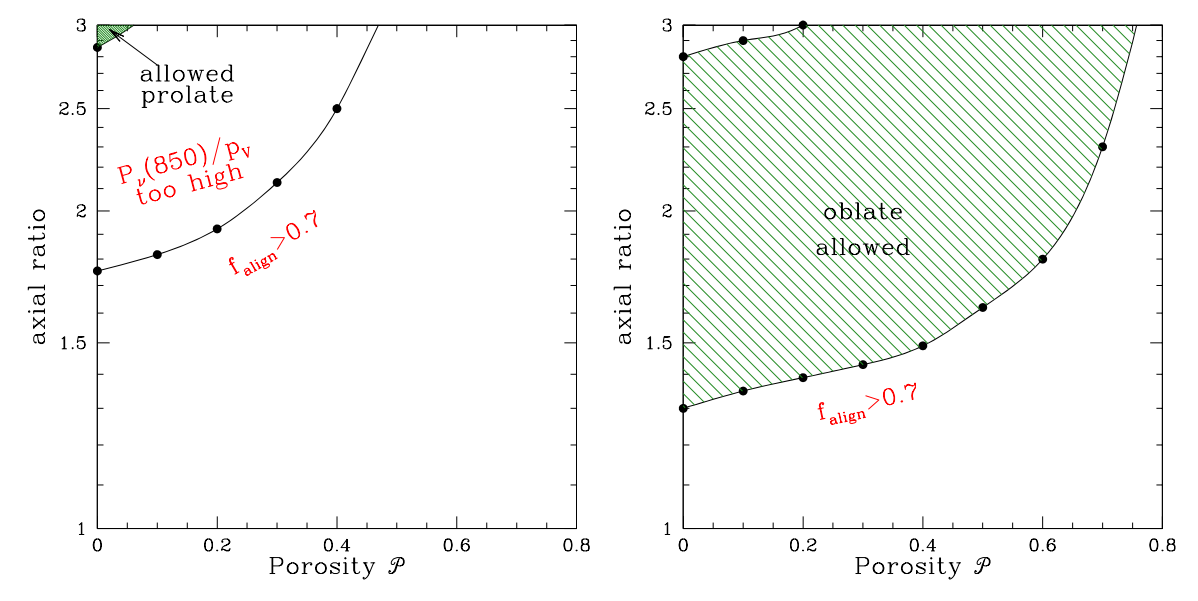


Figure 13. The panels summarize the allowed solutions shown in Figure 12. Green hatched regions show allowed axial ratios for prolate and oblate spheroids. Prolate shapes are limited to a small region (containing the a/b = 3, $\mathcal{P} = 0$ case) in the upper left corner of the left figure.

Figure 12) are shown with filled symbols. Viable models include both oblate and prolate shapes.

Figure 13 shows our estimate of currently "allowed" values of axial ratio and porosity for prolate and oblate shapes. For prolate spheroids with aspect ratio $a/b \le 3$, high porosities are

excluded; the porosity $\mathcal{P} < 0.1$. For oblate spheroids, somewhat larger porosities are allowed, but the porosity is still limited to $\mathcal{P} \lesssim 0.75$. While we do find one viable prolate model (see left panel in Figure 13), it is highly elongated (a/b=3) and the porosity is limited to $\mathcal{P}=0$. It is evident that oblate

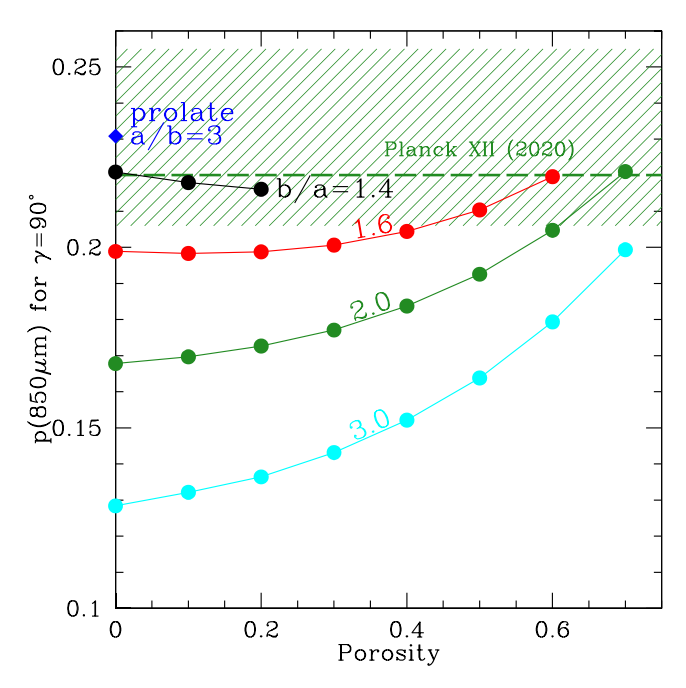


Figure 14. Maximum fractional polarization at 850 μ m for astrodust models using different porosities \mathcal{P} and axial ratios b/a. Model results are shown only for models considered viable based on the ability to reproduce starlight polarization (see Figure 10) and $P_{\nu}(850 \ \mu\text{m})/p_V$ (see Figure 12). The green hatched area shows the Planck Collaboration XII. (2020) result for the limiting value

shapes are preferred. The processes that determine the shapes of interstellar grains evidently favor flattened rather than needle-like geometries.

The fractional polarization of the astrodust emission is

$$p(\lambda) = \frac{C_{\text{pol}}^{\text{MPFA}}(\lambda)}{C_{\text{ext}}^{\text{MPFA}}(\lambda)} = \left[\frac{\langle f_{\text{align}} \rangle C_{\text{pol}} \sin^2 \gamma}{C_{\text{ran}} + \langle f_{\text{align}} \rangle (\cos^2 \gamma - \frac{1}{3}) C_{\text{pol}}} \right],$$
(62)

$$[p(\lambda)]_{Ad} = \frac{0.61(1 - \mathcal{P})}{\Phi_{Ad}^{MPFA}} \left[\frac{C_{pol}(\lambda)}{C_{ran}(\lambda)} \right]_{Ad}$$
$$\frac{\sin^2 \gamma}{1 + \langle f_{align} \rangle_{Ad} (\cos^2 \gamma - \frac{1}{3}) (C_{pol}/C_{ran})_{Ad}}, \tag{63}$$

where Equation (57) has been used, and $C_{\rm aniso} = C_{\rm pol}$ for $a_{\rm eff}/\lambda \ll 1$.

Evaluating Equation (63) for $\gamma = 90^{\circ}$ gives the maximum fractional polarization, shown in Figure 14 for different porosities \mathcal{P} and different axis ratios. The hatched zone shows the Planck Collaboration XII. (2020) result $(22.0^{+3.5}_{-1.4})\%$ based on the 99.9th percentile of observations at 80' resolution. Many of the models that we consider viable fall below 20%, whereas Planck XII claims the peak polarization should be at least 20.6%. Models with the lower fractional polarization would be ruled out if we used only the Planck Collaboration XII. (2020) determination of $P_{\nu}(850 \,\mu\text{m})/p_{V}$, but we allow lower values based on the results of Panopoulou et al. (2019). However, we note that some of our models (e.g., oblate with b/a = 1.4, $\mathcal{P} \leqslant 0.2$) fall comfortably within the green hatched area in Figure 14. It is also worth noting that Draine & Hensley (2021) found that $1.4 \le b/a \le 1.6$ models with low porosity give good fits to the 10 μ m polarization profile.

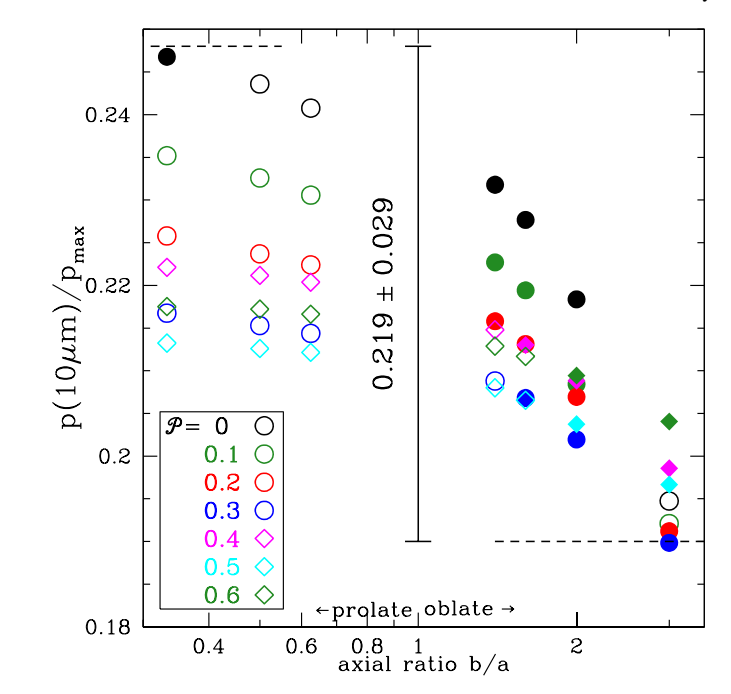


Figure 15. Predicted ratio of 10 μ m polarization to peak optical polarization p_{max} for astrodust spheroids with selected porosity \mathcal{P} and selected axial ratios b/a. Filled symbols denote allowed cases (see Figure 12).

It is also possible that the dust in the regions showing the very highest Planck polarization fractions (the 99.9th percentile) may differ from the "average" diffuse ISM dust that we are trying to capture with our model. The model favored by GFV18 has a peak polarized fraction of 13% (Guillet et al.2018).

11. Silicate 10 μ m Feature Polarization

If the astrodust grains are aligned, the silicate absorption features at 10 and 18 μm will be polarized. Here we calculate the ratio of $p(10~\mu m)$ to the optical polarization $p_{\rm max}$. Combining

$$p(10 \,\mu\text{m}) = N_{\text{H}} V_{\text{align,Ad}} \times \left[\frac{C_{\text{pol}}(10 \,\mu\text{m})}{V} \right]_{\text{Ad}} \sin^2 \gamma \quad (64)$$

with Equations (48) and (54), we obtain

$$\frac{p(10 \ \mu\text{m})}{p_{\text{max}}} = \frac{\Pi_{\text{obs}}/p_{\text{max}}}{\Phi_{\text{Ad}}^{\text{MPFA}}} \times \left[\frac{C_{\text{pol}}(10 \ \mu\text{m})}{V}\right]_{\text{Ad}}.$$
 (65)

Figure 15 shows the prediction for $p(10 \mu \text{m})/p_{\text{max}}$ for different axial ratios b/a and porosities \mathcal{P} . For the porosities $\mathcal{P} \lesssim 0.5$ and axial ratios that are consistent with the observed polarization of starlight and polarized submillimeter emission (see Figure 13; filled symbols in Figure 15), we estimate that

$$\frac{p(10 \ \mu\text{m})}{p_{\text{max}}} \approx 0.219 \pm 0.029 \tag{66}$$

for $\Pi_{\rm obs}/p_{\rm max} \approx 1.23~\mu{\rm m}$ (see Table 1).

To date, there do not appear to be any published measurements of $p(10~\mu\text{m})$ for sightlines where the optical polarization p_{max} has also been measured. The sightline to Cyg OB2-12 has $p_{\text{max}} \approx p(0.43~\mu\text{m}) = 0.0967 \pm 0.0010$ (Whittet et al. 1992), and thus we predict $p(10~\mu\text{m}) \approx 0.021 \pm 0.003$ for Cyg OB2-12.

Measuring $p(10 \mu m)$ for Cyg OB2-12 will be a valuable observational test for the hypothesis that the starlight polarization, silicate absorption, and submillimeter emission arise from a single dominant grain type ("astrodust").

12. Discussion

Following the discovery of starlight polarization (Hiltner 1949b, 1949a; Hall 1949), it has been evident that interstellar grains must be both appreciably nonspherical and aligned, and efforts have been made to determine what grain shapes are required to account for the polarization. Kim & Martin (1995) showed that starlight polarization could be produced by oblate spheroids with axial ratio $b/a \ge 1.414$ or prolate spheroids with $a/b \ge 2$.

Polarization of the 10 μ m silicate feature seen in extinction has provided additional constraints on the grain shape. Martin (1975) argued that the 8–13 μ m polarization of the BN object measured by Dyck et al. (1973) and Dyck & Beichman (1974) required b/a > 1.5 if the grains were oblate, and a/b > 2.5 if they were prolate. Lee & Draine (1985) argued that the 8–13 μ m polarization of the BN object measured by Capps (1976) was well fitted by 2:1 oblate grains; this was confirmed by Hildebrand (1988) using newer observations by Aitken et al. (1985). Aitken et al. (1989) obtained additional spectropolarimetry of BN, extending coverage to include the silicate feature at 20 μ m; they also concluded that 2:1 oblate grains were consistent with the 10 μ m feature, although the observed $20 \,\mu \text{m}$ polarization was stronger than predicted for the astrosilicate dielectric function of Draine & Lee (1984). Hildebrand & Dragovan (1995) added far-infrared constraints, observing 100 μ m polarizations as large as 9% from starforming clouds, which they argued was consistent with thermal emission from 1.5:1 oblate grains.

The Planck mission (Planck Collaboration I. 2011) provided measurements of polarized submillimeter emission from dust from the diffuse ISM, observing fractional polarizations at 353 GHz sometimes exceeding 20% (Planck Collaboration XII. 2020). Guillet et al. (2018, hereafter GFV18) developed models using spheroids of amorphous silicate and amorphous carbon (a-C) to reproduce both starlight polarization and polarized submillimeter emission. Both GFV18 and the present paper assume a population of "large" grains plus a population of polycyclic aromatic hydrocarbon (PAH) nanoparticles. However, GFV18 differed from the present paper in several respects. For the large particles, GFV18 assumed silicate and a-C grains. The silicate grains were modeled using the "astrosilicate" dielectric function from Weingartner & Draine (2001), with long-wavelength modifications from Li & Draine (2001). The a-C grains were modeled using optical constants of "BE" amorphous carbon from Zubko et al. (1996). Also considered by GFV18 was a model with astrosilicate and a-C mixed in the same grains.

The present study assumes a population of "astrodust" grains incorporating both silicate and carbonaceous material, with an effective dielectric function depending on assumed porosity, derived as discussed by Draine & Hensley (2021). These astrodust grains (plus a population of nanoparticles, including PAHs) are able to reproduce the observed interstellar extinction (including polarization) from the far-UV to $\sim\!30~\mu\text{m}$, as well as emission (including polarization) from the mid-IR to the submillimeter (B. S. Hensley & B. T. Draine 2021, in preparation).

Despite the differences in assumptions of the two studies, similar conclusions are reached: model D of GFV18 has aligned a-C grains that are prolate with axial ratio 3:1 and aligned mixed silicate+a-C grains that are prolate with axial ratio 2.5:1. Here we show that the observed starlight polarization integral Π_{obs} and polarized submillimeter emission can be reproduced by "astrodust" spheroids with suitable shape and porosity. Viable cases (see Figure 13) include 3:1 prolate spheroids for $\mathcal{P} < 0.1$, 1.4:1 oblate spheroids with $\mathcal{P} < 0.3$, or 2:1 oblate spheroids with $\mathcal{P} < 0.65$. GFV18 did not apply the color correction factor of 1.11 used here to convert Planck 353 GHz band measurements to monochromatic 353 GHz intensities. We find that this 11% reduction in observed polarized intensity rules out a number of our prolate models (see Figure 12). The present study has only used an integral over the starlight polarization as a constraint, allowing us to more thoroughly explore parameter space (shape and porosity); future studies (B. S. Hensley & B. T. Draine 2021, in preparation) will employ models with detailed size distributions that reproduce the wavelength dependence of both extinction and polarization.

One important conclusion of the present study is that extreme porosities are excluded. High-porosity grains are inefficient polarizers, for both starlight attenuation and thermal emission. Models using spheroids with axial ratios ≤ 3 are able to reproduce the observed polarization of starlight only for porosity $\mathcal{P} \lesssim 0.5$ for prolate shapes, or $\mathcal{P} \lesssim 0.75$ for oblate shapes (see Figure 13). Some authors (e.g., Mathis & Whiffen 1989; Fogel & Leung 1998; Min et al. 2006; Ormel et al. 2011; Ysard et al. 2018) have proposed that interstellar grains may be highly porous as a result of coagulation processes. However, we find here that the observed polarization of starlight, together with the strongly polarized thermal emission at submillimeter wavelengths, allows strong limits to be placed on the porosity. If the dust consists of either oblate or prolate spheroids with long:short axial ratios $\leq 2:1$, the porosity of the dust cannot exceed 65%. While low-velocity coagulation may tend to form "fluffy" structures, perhaps a combination of fragmentation and compression in higher-velocity collisions keeps the "porosity" of the dust population low.

The present work has been limited to a single family of very simple grain shapes: spheroids. The combination of starlight polarization and submillimeter polarization can be reproduced with only certain axial ratios and porosities (Figure 13). This in turn leads to a prediction for the polarization in the 10 μ m feature: $p(10 \, \mu\text{m})/p_V = 0.219 \pm 0.029$. How the ratio of submillimeter polarization (grain in the Rayleigh limit) to optical polarization (grain size comparable to the wavelength) might vary for other grain geometries is not yet known, nor is how this might impact predictions for $p(10 \, \mu\text{m})/p_V$.

It has been suggested that interstellar grains may contain metallic Fe inclusions (e.g., Jones & Spitzer 1967; Martin 1995). The "astrodust" dielectric function (Draine & Hensley 2021) used here implicitly allows for the contributions of any such inclusions to the "effective" dielectric function, provided only that the inclusions are small compared to the wavelength. The only complication arises at frequencies $\lesssim 100$ GHz, where ferromagnetic inclusions might contribute magnetic dipole radiation with "negative" polarization (Draine &

 $[\]overline{^{7}}$ For example, Ormel et al. (2011) considered aggregates with porosities as large as $\mathcal{P}=0.9$, and Min et al. (2006) considered some aggregates with $\mathcal{P}>0.99$.

Hensley 2013), but the present discussion has not used observations below 353 GHz.

Our understanding of grain shape can be expected to advance as more measurements of starlight polarization become available—both the wavelength dependence for additional sightlines (Bagnulo et al. 2017), as well as measurements of starlight polarization p_V for large numbers of stars (e.g., PASIPHAE; Tassis et al. 2018) to allow determination of $P_{\nu}(850 \ \mu m)/p_V$ for many more sightlines.

The power of the present study has been limited by uncertainty regarding the actual value of $P_{\nu}(850~\mu\text{m})/p_{V}$. The Planck result for $P_{\nu}(850~\mu\text{m})/p_{V}$ is ~29% larger than the PHS19 value for selected sightlines; this range of values translates into an enlarged domain of allowed values in the axial ratio–porosity plane. Further studies of $P_{\nu}(850~\mu\text{m})/p_{V}$ using starlight polarization measurements on additional sightlines will be valuable. If $P_{\nu}(850~\mu\text{m})/p_{V}$ shows regional or environmental variations (beyond what can be attributed to variations in grain temperature), this would be an important clue toward understanding the evolution of dust in the ISM.

Finally, we note that the profile of the $10 \,\mu m$ silicate feature in polarization provides valuable constraints on shape and porosity (Draine & Hensley 2021). Unfortunately, existing spectropolarimetry of this feature in the diffuse ISM is limited (Wright et al. 2002). High signal-to-noise ratio measurements of the $10 \,\mu m$ silicate polarization profile would help to better constrain the porosity and shape of interstellar grains.

13. Summary

The principal results of this study are as follows.

- 1. The accuracy of the MPFA is tested at optical wavelengths. The MPFA (Equations (24) and (25)) provides an adequate approximation to the orientationally averaged polarization and extinction cross sections for spinning and precessing submicron grains. At long wavelengths $\lambda \gg a_{\rm eff}$, the MPFA is highly accurate.
- 2. The polarization efficiency integral Φ (Equation (29)) is introduced to measure the effectiveness of grains for polarizing starlight. We evaluate $\Phi_{\rm Ad}^{\rm MPFA}(b/a,\,a_{\rm eff})$ for astrodust spheroids (see Figure 9) with porosities from $\mathcal{P}=0$ to 0.9.
- 3. The fraction of the dust mass that is aligned, $\langle f_{\rm align} \rangle$, can be estimated from the observed starlight polarization integral $\Pi_{\rm obs}({\rm Equation~(35)})$ and the polarization efficiency integral Φ , without having to fit a size distribution of aligned grains to the wavelength dependence of starlight polarization.
- 4. Assuming astrodust grains with spheroidal shapes, the limit $\langle f_{\rm align} \rangle_{\rm Ad} < 0.70$, together with the starlight polarization integral $\Pi_{\rm obs}$ and the polarization efficiency integral $\Phi_{\rm Ad}^{\rm MPFA}$, constrains the aspect ratio of the dust grains producing the starlight polarization. If the grains have low porosity, then axial ratios a/b > 1.8 are required if the grains are prolate spheroids, and axial ratios b/a > 1.4 are required if the grains are oblate spheroids. If the grains are substantially porous, then more extreme axial ratios would be required: $a/b \gtrsim 2.5$ or $b/a \gtrsim 1.5$ for $\mathcal{P}=0.4$ (see Figure 10).
- 5. For spheroids with axial ratios \leqslant 3, the limit $\langle f_{\rm align} \rangle_{\rm Ad} < 0.7$ and the observed starlight polarization imply that extreme porosities $\mathcal{P} \gtrsim 0.75$ are excluded.

- 6. The ratio of polarized submillimeter emission to starlight polarization provides an additional constraint on porosity and grain shape. We combine this with the limit $\langle f_{\rm align} \rangle_{\rm Ad} < 0.7$ to determine the domain of allowed spheroid shapes and porosities (Figure 13). Almost all models with prolate grains are excluded, while a wide range of oblate grains with axial ratio $b/a \gtrsim 1.4$ are viable.
- 7. We calculate the expected ratio of 10 μ m polarization to visual polarization p_V if the grains can be approximated by spheroids and the optical extinction, 10 μ m polarization, and submillimeter polarization all arise from the same grains. We predict $p(10 \, \mu\text{m})/p_V = 0.219 \pm 0.029$. For Cyg OB2-12, we predict $p(10 \, \mu\text{m}) \approx (2.1 \pm 0.3)\%$.

This work was supported in part by NSF grants AST-1408723 and AST-1908123 and carried out in part at the Jet Propulsion Laboratory, California Institute of Technology, under a contract with the National Aeronautics and Space Administration. We thank Francois Boulanger and Vincent Guillet for helpful discussions. We particularly thank the referee, Peter G. Martin, for extensive and helpful comments that led to an improved manuscript. We thank Robert Lupton for the availability of the SM package, and the late Nicolai Voshchinnikov for very generously making available the separation of variables code hom6_5q.

Appendix A General Orientational Averages

Consider a rotationally symmetric grain with symmetry axis \hat{a} and angular momentum $J = J \hat{j}$, with

$$\hat{\boldsymbol{j}} = j_x \hat{\boldsymbol{x}} + j_y \hat{\boldsymbol{y}} + j_z \hat{\boldsymbol{z}}. \tag{A1}$$

Let α be the angle between \hat{j} and \hat{a} (see Figure 1). If $\alpha \neq 0$, then \hat{a} precesses around \hat{j} :

$$\hat{\boldsymbol{a}} = \cos \alpha \, \hat{\boldsymbol{j}} + \sin \alpha \cos \beta \, \frac{(j_z \hat{\boldsymbol{y}} - j_y \hat{\boldsymbol{z}})}{(j_y^2 + j_z^2)^{1/2}}$$

$$+ \sin \alpha \sin \beta \, \hat{\boldsymbol{j}} \times \frac{(j_z \hat{\boldsymbol{y}} - j_y \hat{\boldsymbol{z}})}{(j_y^2 + j_z^2)^{1/2}},$$
(A2)

where the free precession angle β varies from zero to 2π . Thus,

$$\hat{\boldsymbol{a}} \cdot \hat{\boldsymbol{x}} = \cos \alpha \, j_x - \sin \alpha \sin \beta \, (j_y^2 + j_z^2)^{1/2}, \tag{A3}$$

$$\hat{a} \cdot \hat{y} = \cos \alpha j_{y} + \sin \alpha \cos \beta \frac{j_{z}}{(j_{y}^{2} + j_{z}^{2})^{1/2}} + \sin \alpha \sin \beta \frac{j_{x} j_{y}}{(j_{y}^{2} + j_{z}^{2})^{1/2}},$$
(A4)

$$\hat{a} \cdot \hat{z} = \cos \alpha j_z - \sin \alpha \cos \beta \frac{j_y}{(j_y^2 + j_z^2)^{1/2}} + \sin \alpha \sin \beta \frac{j_x j_z}{(j_y^2 + j_z^2)^{1/2}}.$$
 (A5)

Let the magnetic field $\mathbf{B}_0 = B_0 \hat{\mathbf{b}}$ be in the $\hat{\mathbf{x}} - \hat{\mathbf{z}}$ plane:

$$\hat{\boldsymbol{b}} = \sin\gamma\,\hat{\boldsymbol{x}} + \cos\gamma\,\hat{\boldsymbol{z}}.\tag{A6}$$

Magnetic torques will cause \hat{j} to precess around \hat{b} . Let ψ be the angle between \hat{j} and B_0 . Then,

$$j_x = \sin\gamma\cos\psi + \cos\gamma\sin\psi\cos\xi,\tag{A7}$$

$$j_{v} = \sin \psi \sin \xi, \tag{A8}$$

$$j_z = \cos\gamma\cos\psi - \sin\gamma\sin\psi\cos\xi,\tag{A9}$$

where the magnetic precession angle ξ runs from zero to 2π .

The orientation of the spheroid is determined by the orientation of the symmetry axis \hat{a} . Consider light propagating with $\hat{k} = \hat{z}$. Let Θ be the angle between \hat{k} and \hat{a} , and let $(C_E(\Theta), C_H(\Theta))$ be cross sections for linearly polarized light with $E(\parallel, \perp)$ to the $\hat{k} - \hat{a}$ plane. For a given α and ψ , the time-averaged cross sections for light linearly polarized in the \hat{x} and \hat{y} directions are obtained by integrating over the spin angle β and magnetic precession angle ξ :

$$\langle C_x \rangle = \int_0^{2\pi} \frac{d\beta}{2\pi} \int_0^{2\pi} \frac{d\xi}{2\pi} \left[\frac{(\hat{\boldsymbol{a}} \cdot \hat{\boldsymbol{x}})^2 C_E(\Theta) + (\hat{\boldsymbol{a}} \cdot \hat{\boldsymbol{y}})^2 C_H(\Theta)}{(\hat{\boldsymbol{a}} \cdot \hat{\boldsymbol{x}})^2 + (\hat{\boldsymbol{a}} \cdot \hat{\boldsymbol{y}})^2} \right], \tag{A10}$$

$$\langle C_{y} \rangle = \int_{0}^{2\pi} \frac{d\beta}{2\pi} \int_{0}^{2\pi} \frac{d\xi}{2\pi} \left[\frac{(\hat{\boldsymbol{a}} \cdot \hat{\boldsymbol{x}})^{2} C_{H}(\Theta) + (\hat{\boldsymbol{a}} \cdot \hat{\boldsymbol{y}})^{2} C_{E}(\Theta)}{(\hat{\boldsymbol{a}} \cdot \hat{\boldsymbol{x}})^{2} + (\hat{\boldsymbol{a}} \cdot \hat{\boldsymbol{y}})^{2}} \right]. \tag{A11}$$

The factors $(\hat{a} \cdot \hat{x})^2$ and $(\hat{a} \cdot \hat{y})^2$ depend on β and ψ , and so does

$$\Theta = \arccos \left[\cos \alpha j_z - \sin \alpha \cos \beta \frac{j_y}{(j_y^2 + j_z^2)^{1/2}} + \sin \alpha \sin \beta \frac{j_x j_z}{(j_y^2 + j_z^2)^{1/2}} \right]. \tag{A12}$$

For direct evaluation of the averages (Equations (A10) and (A11)), we first tabulate $C_E(\Theta)$ and $C_H(\Theta)$ for a grid of values of $0 \le \Theta \le 90^{\circ}$ and obtain $C_E(\Theta)$ and $C_H(\Theta)$ by interpolation. For the special case $\alpha = 0$, the quantities $\hat{\boldsymbol{a}} \cdot \hat{\boldsymbol{x}}$, $\hat{\boldsymbol{a}} \cdot \hat{\boldsymbol{y}}$, and Θ are

independent of β , and Equations (A10) and (A11) reduce to integrals over ξ .

Appendix B Averages for the MPFA

For the MPFA, we use certain averages over the free precession angle β :

$$\langle (\hat{\boldsymbol{a}} \cdot \hat{\boldsymbol{x}})^2 \rangle_{\beta} = \cos^2 \alpha \, j_x^2 + \frac{1}{2} \sin^2 \alpha \, (j_y^2 + j_z^2), \tag{B13}$$

$$\langle (\hat{\boldsymbol{a}} \cdot \hat{\boldsymbol{y}})^2 \rangle_{\beta} = \cos^2 \alpha \, j_y^2 + \frac{1}{2} \sin^2 \alpha (1 - j_y^2), \tag{B14}$$

$$\langle (\hat{\boldsymbol{a}} \cdot \hat{\boldsymbol{z}})^2 \rangle_{\beta} = \cos^2 \alpha \, j_z^2 + \frac{1}{2} \sin^2 \alpha (1 - j_z^2), \tag{B15}$$

where j_x , j_y , and j_z are given by Equations (A7)–(A9). In the Rayleigh limit, $C_E(\Theta)$ and $C_H(\theta)$ are taken to be given by Equations (15) and (16), and all we require is the average over the angles (α, ψ) :

$$\langle R \rangle \equiv \left\langle \left[\frac{3}{2} \cos^2 \alpha - \frac{1}{2} \right] \left[\frac{3}{2} \cos^2 \psi - \frac{1}{2} \right] \right\rangle_{\alpha, \psi}.$$
 (B16)

Figures 3 and 4 show orientation-averaged cross sections for polarization and extinction by 2:1 astrodust spheroids with porosity $\mathcal{P}=0$ and $a_{\rm eff}=0.15~\mu \rm m$. The MPFA is seen to be exact at long wavelengths and to provide $\sim \! 10\%$ accuracy near the peak of the polarization and extinction.

Figures 16 and 17 show orientationally averaged cross sections for astrodust with porosity $\mathcal{P}=0.5$ and $a_{\rm eff}=0.25~\mu{\rm m}$. The results are qualitatively similar to what was seen in Figures 3 and 4. The polarization efficiency factors $Q_{\rm pol} \equiv C_{\rm pol}/\pi a_{\rm eff}^2$ in Figure 16 are significantly smaller than the results in Figure 3 for $\mathcal{P}=0$.

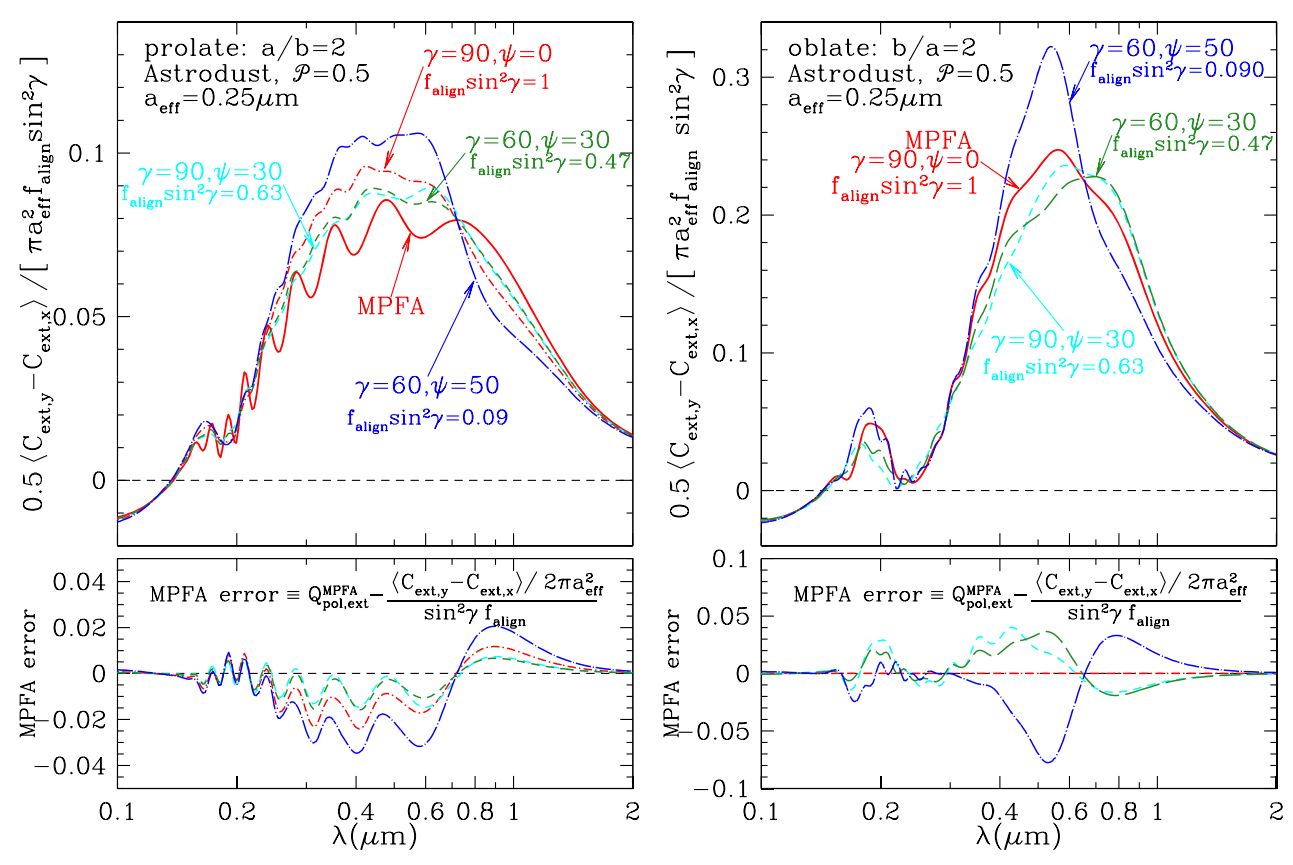


Figure 16. Orientationally averaged cross section for polarization $(1/2)(\langle C_x \rangle - \langle C_y \rangle)$ divided by $\pi a_{\rm eff}^2 f_{\rm align} \sin^2 \gamma$ as a function of wavelength λ for astrodust with porosity $\mathcal{P}=0.5$ and $a_{\rm eff}=0.25$ $\mu \rm m$. Left: 2:1 prolate grains. Right: 2:1 oblate grains. Grains are spinning with J parallel to the principal axis of the largest moment of inertia (prolate: $\alpha=\pi/2$; oblate: $\alpha=0$), with J precessing around B_0 . Results are shown for four distributions of grain orientation, labeled by $\gamma=0.5$ and the line of sight and $\psi=0.5$ are the matrix of the matrix of $\psi=0.5$ and $\psi=$

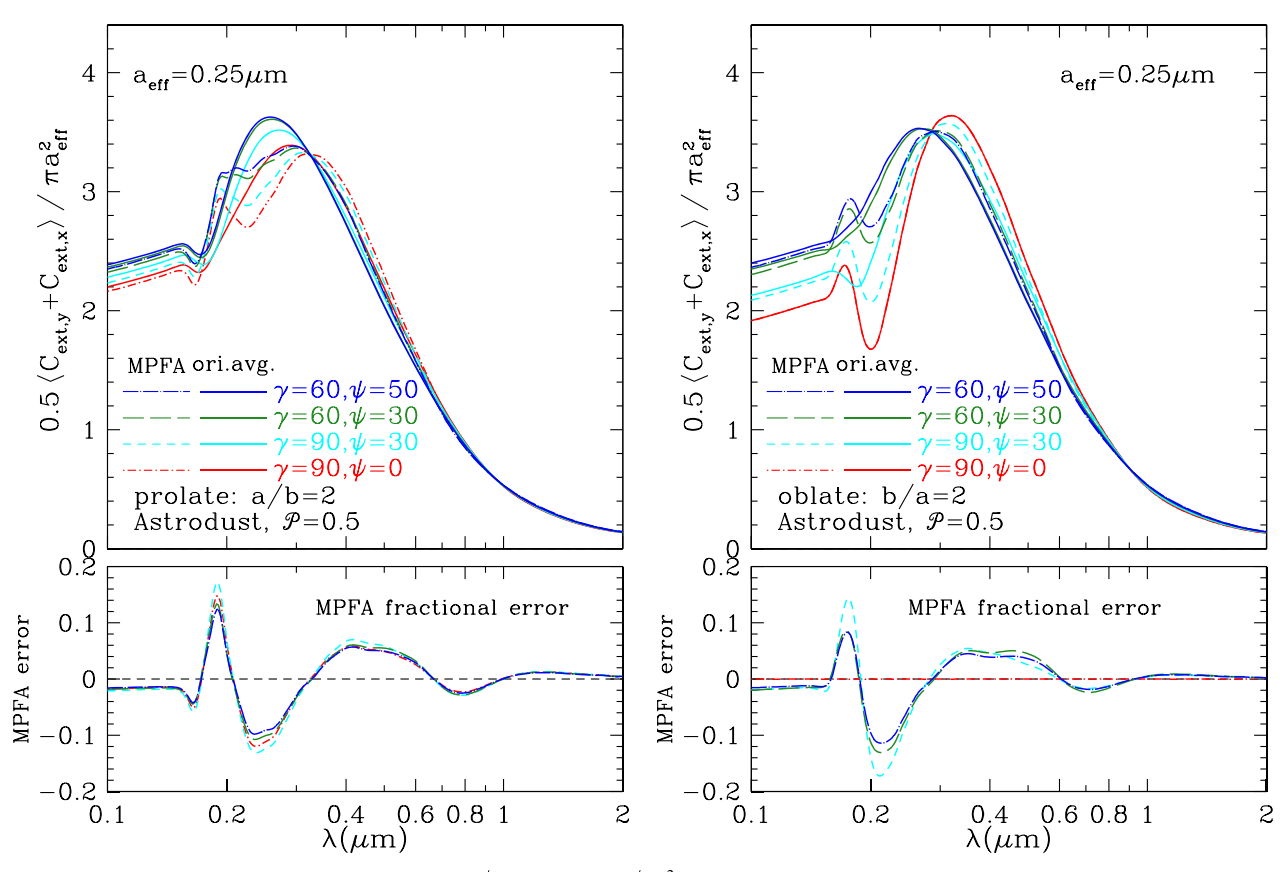


Figure 17. Orientationally averaged extinction efficiency $(1/2)(\langle C_x \rangle + \langle C_y \rangle)/\pi a_{\rm eff}^2$ as a function of wavelength λ for astrodust with porosity $\mathcal{P}=0.5$ and $a_{\rm eff}=0.25~\mu \rm m$. Left: 2:1 prolate grains. Right: 2:1 oblate grains. Grains are spinning with J parallel to the principal axis of the largest moment of inertia $(\alpha=\pi/2)$ for prolate, $\alpha=0$ for oblate) with J precessing around B_0 . Results are shown for four distributions of grain orientation, labeled by $\gamma=$ angle between B_0 and the line of sight and $\psi=$ angle between J and J0. Curves labeled "MPFA" correspond to the MPFA. Lower panels show the error in $(\langle C_y \rangle + \langle C_x \rangle)/2\pi a_{\rm eff}^2$ if the MPFA is used. Errors are both positive and negative and will tend to average out for size distributions.

ORCID iDs

B. T. Draine https://orcid.org/0000-0002-0846-936X Brandon S. Hensley https://orcid.org/0000-0001-7449-4638

References

```
Aitken, D. K., Bailey, J. A., Roche, P. F., & Hough, J. M. 1985, MNRAS,
   215, 815
Aitken, D. K., Smith, C. H., & Roche, P. F. 1989, MNRAS, 236, 919
Al-Rizzo, H. M., & Tranquilla, J. M. 1995, JCoPh, 119, 342
Andersson, B.-G., Lazarian, A., & Vaillancourt, J. E. 2015, ARA&A, 53, 501
Asano, S., & Yamamoto, G. 1975, ApOpt, 14, 29
Bagnulo, S., Cox, N. J. L., Cikota, A., et al. 2017, A&A, 608, A146
Capps, R. W. 1976, PhD thesis, Univ. of Arizona, Tucson
Davis, L. J., & Greenstein, J. L. 1951, ApJ, 114, 206
Dolginov, A. Z., & Mytrophanov, I. G. 1976, Ap&SS, 43, 291
Draine, B. T., & Allaf-Akbari, K. 2006, ApJ, 652, 1318
Draine, B. T., & Flatau, P. J. 1994, JOSAA, 11, 1491
Draine, B. T., & Fraisse, A. A. 2009, ApJ, 696, 1
Draine, B. T., & Hensley, B. 2013, ApJ, 765, 159
Draine, B. T., & Hensley, B. S. 2021, ApJ, 909, 94
Draine, B. T., & Lee, H. M. 1984, ApJ, 285, 89
Draine, B. T., & Weingartner, J. C. 1997, ApJ, 480, 633
Dyck, H. M., & Beichman, C. A. 1974, ApJ, 194, 57
Dyck, H. M., Capps, R. W., Forrest, W. J., & Gillett, F. C. 1973, ApJL,
Fanciullo, L., Guillet, V., Boulanger, F., & Jones, A. P. 2017, A&A, 602, A7
Fogel, M. E., & Leung, C. M. 1998, ApJ, 501, 175
Greenberg, J. M. 1968, in Interstellar Grains, ed. B. M. Middlehurst &
   L. H. Aller (Chicago, IL: The Univ. of Chicago Press), 221
Guillet, V., Fanciullo, L., Verstraete, L., et al. 2018, A&A, 610, A16
```

```
Hall, J. S. 1949, Sci, 109, 166
Hensley, B. S., & Draine, B. T. 2020, ApJ, 895, 38
Hensley, B. S., & Draine, B. T. 2021, ApJ, 906, 73
Hensley, B. S., Zhang, C., & Bock, J. J. 2019, ApJ, 887, 159
Hildebrand, R. H. 1988, QJRAS, 29, 327
Hildebrand, R. H., & Dragovan, M. 1995, ApJ, 450, 663
Hiltner, W. A. 1949a, Sci, 109, 165
Hiltner, W. A. 1949b, Natur, 163, 283
Jones, R. V., & Spitzer, L. J. 1967, ApJ, 147, 943
Kim, S.-H., & Martin, P. G. 1995, ApJ, 444, 293
Landau, L. D., & Lifshitz, E. M. 1976, Mechanics (Oxford: Pergamon Press)
Lee, H. M., & Draine, B. T. 1985, ApJ, 290, 211
Lenz, D., Hensley, B. S., & Doré, O. 2017, ApJ, 846, 38
Li, A., & Draine, B. T. 2001, ApJ, 554, 778
Martin, P. G. 1975, ApJ, 202, 393
Martin, P. G. 1995, ApJL, 445, L63
Martin, P. G., Clayton, G. C., & Wolff, M. J. 1999, ApJ, 510, 905
Martin, P. G., & Whittet, D. C. B. 1990, ApJ, 357, 113
Mathis, J. S., Rumpl, W., & Nordsieck, K. H. 1977, ApJ, 217, 425
Mathis, J. S., & Whiffen, G. 1989, ApJ, 341, 808
Min, M., Dominik, C., Hovenier, J. W., de Koter, A., & Waters, L. B. F. M.
   2006, A&A, 445, 1005
Mishchenko, M. I. 2000, ApOpt, 39, 1026
Mishchenko, M. I. 2020, JOSRT, 242, 106692
Ormel, C. W., Min, M., Tielens, A. G. G. M., Dominik, C., & Paszun, D. 2011,
   A&A, 532, A43
Panopoulou, G. V., Hensley, B. S., Skalidis, R., Blinov, D., & Tassis, K. 2019,
     &A, 624, L8
Planck Collaboration I. 2011, A&A, 536, A1
Planck Collaboration XII. 2020, A&A, 641, A12
Planck Collaboration Int. XIX. 2015, A&A, 576, A104
Planck Collaboration Int. XX. 2015, A&A, 576, A105
Planck Collaboration Int. XXII. 2015, A&A, 576, A107
```

```
Planck Collaboration Int. XLVIII. 2016, A&A, 596, A109
Purcell, E. M. 1975, in The Dusty Universe, ed. G. B. Field & A. G. W. Cameron (New York: Neale Watson Academic), 155
Purcell, E. M. 1979, ApJ, 231, 404
Rogers, C., & Martin, P. G. 1979, ApJ, 228, 450
Serkowski, K. 1973, in IAU Symp. 52: Interstellar Dust and Related Topics, ed. J. M. Greenberg & H. C. van de Hulst (Dordrecht: Reidel), 145
Serkowski, K., Mathewson, D. S., & Ford, V. L. 1975, ApJ, 196, 261
Siebenmorgen, R., Voshchinnikov, N. V., & Bagnulo, S. 2014, A&A, 561, A82
Smith, C. H., Wright, C. M., Aitken, D. K., Roche, P. F., & Hough, J. H. 2000,
```

Smith, C. H., Wright, C. M., Aitken, D. K., Roche, P. F., & Hough, J. H. 2000 MNRAS, 312, 327

Tassis, K., Ramaprakash, A. N., Readhead, A. C. S., et al. 2018, arXiv:1810. 05652

Voshchinnikov, N. V., & Farafonov, V. G. 1993, Ap&SS, 204, 19

```
Waterman, P. C. 1965, Proc. IEEE, 53, 805
Weingartner, J. C., & Draine, B. T. 2001, ApJ, 548, 296
Weingartner, J. C., & Jordan, M. E. 2008, ApJ, 672, 382
Weingartner, J. C., Kolasi, E., & Woods, C. 2021, MNRAS, 504, 1164
Whittet, D. C. B. 2003, Dust in the Galactic Environment (II edn.; Bristol: Institute of Physics (IOP) Publishing)
Whittet, D. C. B., Martin, P. G., Hough, J. H., et al. 1992, ApJ, 386, 562
Wright, C. M., Aitken, D. K., Smith, C. H., Roche, P. F., & Laureijs, R. J. 2002, in in The Origin of Stars and Planets: The VLT View, 85 ed. J. F. Alves & M. J. McCaughrean (Berlin: Springer)
Ysard, N., Jones, A. P., Demyk, K., Boutéraon, T., & Koehler, M. 2018, A&A, 617, A124
Zubko, V., Dwek, E., & Arendt, R. G. 2004, ApJS, 152, 211
```

Zubko, V., Dwek, E., & Arendt, R. G. 2004, ApJS, 132, 211

Zubko, V. G., Mennella, V., Colangeli, L., & Bussoletti, E. 1996, MNRAS, 282, 1321

21